Small

NANO · MICRO small
www.small-journal.com

REVIEW

Progress in Halide Perovskites and Their Derivatives for X-Ray Scintillators

Han Xiao[1] | Lingwei Zeng[2] | Daqin Chen[1,3]

[1]College of Physics and Energy, Fujian Normal University, Fuzhou, Fujian, P. R. China | [2]School of Chemistry and Chemical Engineering, Key Laboratory of Theoretical Organic Chemistry and Functional Molecule of Ministry of Education, Hunan University of Science and Technology, Xiangtan, Hunan, P. R. China | [3]Fujian Provincial Engineering Technology Research Center of Solar Energy Conversion and Energy Storage, Fuzhou, Fujian, P. R. China

Correspondence: Daqin Chen (dqchen@fjnu.edu.cn)

Received: 23 December 2025 | **Revised:** 7 May 2026 | **Accepted:** 30 May 2026

Keywords: halide perovskites | light yield | luminescent materials | scintillators

ABSTRACT

Halide perovskites (HPs) and their derivatives are considered as promising candidates for next-generation scintillator materials due to their strong x-ray absorption capability, favorable optoelectronic properties, and relatively low manufacturing costs. This review offers a systematic overview of recent advancements and potential applications of HP scintillators. First, the working mechanism of x-ray detection is explained based on the fundamental physical processes involved in the interaction between x-rays and materials. Second, optimization strategies for key performance parameters such as light yield and response-decay time are summarized, with particular emphasis on techniques for modulating the light transmission. Finally, the major challenges impeding the practical implementation of perovskite scintillators are discussed, and an outlook on potential future developments is provided.

1 | Introduction

Since Wilhelm Conrad Röntgen discovered x-rays in 1895, x-ray detectors have been widely employed in medical imaging, high-energy physics research, security monitoring, and industrial non-destructive testing [1, 2]. According to their detection principles, x-ray detectors are primarily divided into two types: direct and indirect. Guided by an external bias voltage, x-rays are immediately transformed into collectible electrical signals through direct detection. For indirect detectors, the key component is a scintillator, which can convert absorbed high-energy x-rays into ultraviolet-visible light. The light is subsequently detected by a photodetector or photomultiplier tube [3].

Materials like α-Se, Si, CdTe, CdZnTe, PbI_2, and HgI_2 are commonly employed in direct conversion detectors, yet each of them has certain drawbacks. For example, α-Se and Si exhibit low absorption cross-sections and small attenuation coefficients for high-energy x-rays (>50 keV) [4]. CdTe and CdZnTe are limited by high electron trap densities and expensive manufacturing costs [5]. PbI_2 and HgI_2 detectors suffer from large leakage currents and high operating voltages [6, 7]. Currently, scintillators have dominated the commercial market due to their superior detection efficiency. They are mainly categorized into inorganic and organic types. Organic scintillators (including organic crystals, plastics and liquids) serve as a valuable complement to inorganic scintillators, but their applications are constrained by low density and small atomic numbers [8, 9]. The evolution of inorganic scintillation materials can be roughly divided into three stages (Scheme 1). The first stage began in the late 19th century with the use of $CaWO_4$ for detecting radioactive phenomenon, signifying its utilization in high-energy particle detection and research. This period ended with the emergence of photomultiplier tubes. The second stage was initiated by Hofstadters, who discovered the scintillation phenomenon of naphthalene by exciting NaI crystals with Tl. CsI:Tl and NaI:Tl (halide scintillators), BaF_2 (fluoride scintillator), $PbWO_4$ and $Bi_4Ge_3O_{12}$ (BGO) (oxide scintillators) have become widely used scintillators and are frequently

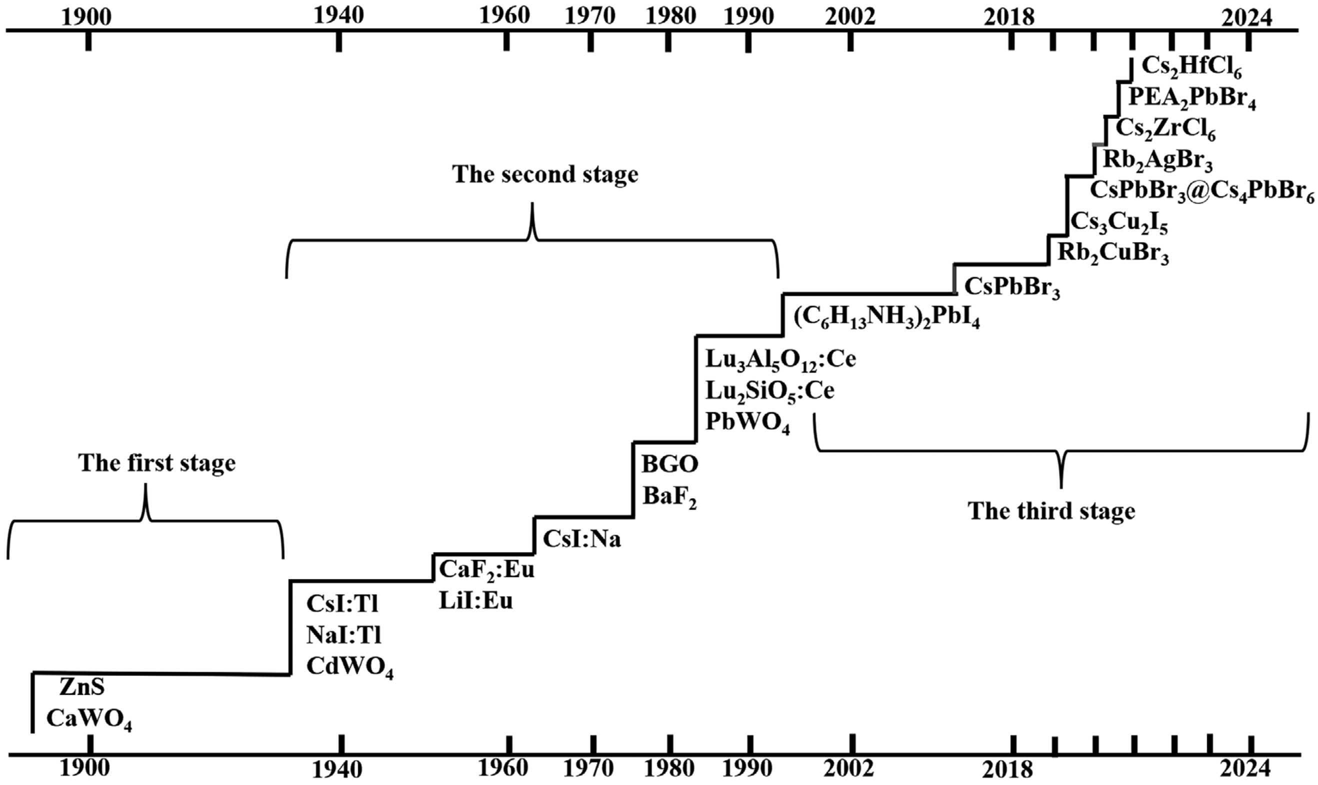

SCHEME 1 | A diagram showing the evolution of different inorganic scintillation materials.

employed as representative benchmarks for evaluating the efficiency of new materials. Nevertheless, these materials still face some challenges. For instance, BGO needs to be synthesized under high-temperature and complex process conditions, making it difficult to obtain large-sized and defect-free crystals [10]. Meanwhile, its brittle nature hinders its application in flexible x-ray imaging [11]. The ceramic Gd_2O_2S (GOS) utilized for x-ray computed tomography (CT) shows a comparatively slow decay time, which affects image quality in dynamic imaging [12, 13]. The performance of CsI:Tl and NaI:Tl imaging systems is compromised over time by their high hygroscopicity [14]. Moreover, most traditional scintillators have inherent radiation luminescence characteristics, and the emission peaks are not well aligned with the optimal spectral response range of photodetectors, thereby limiting the application of multicolor imaging techniques. As the demand for advanced x-ray detection technologies continues to grow, scintillation materials have evolved into the third generation. Traditional scintillators are increasingly unable to meet the requirements of practical applications, highlighting the urgent need for the development of high-performance alternatives.

In recent years, halide perovskites (HPs) and their derivatives have been regarded as the most promising candidates for scintillator materials. The x-ray attenuation coefficient, as one of the core parameters of scintillators, is proportional to $\rho Z_{\mathrm{eff}}^{3-4}$, where ρ denotes the density of the scintillator, and Z_{eff} is the effective atomic number [15]. Higher values of ρ and Z_{eff} enhance the material's ability to attenuate ionizing radiation, improving its suitability for CT imaging. Due to the presence of high atomic number elements such as Pb, Br, and I, HPs display highly efficient x-ray absorption [16–18]. Additionally, they possess excellent optical properties, including nearly 100% photoluminescence quantum yield (PLQY), low trap density, nanosecond decay lifetimes, tunable optical bandgaps, and a relatively straightforward fabrication process [19–22]. Compared with other materials, HPs offer more marked advantages in x-ray detection and imaging fields (Table 1) [18, 23–40]. In 2002, Shibuya et al. first used the organic–inorganic hybrid perovskite $(C_6H_{13}NH_3)_2PbI_4$ as a scintillator for radiation pulse detection, initiating preliminary research on perovskite materials in x-ray detection [41]. Since then, substantial progress has been made in detection sensitivity. The light yield substantially surpasses that of commercial device representatives such as NaI:Tl (38 000 photons/MeV) and BGO (8 500 photons/MeV). Lead-based perovskites like $CsPbBr_3$ display ultrafast decay time, being several orders of magnitude short than BGO (300 ns) and GOS (1200 ns). Thus far, the lowest detection limit has been shown to be 13 $\mathrm{nGy_{air}/s}$, approximately 420 times lower than the standard dose used in clinical x-ray diagnostics [23]. The conversion efficiency of halide perovskite x-ray scintillators can reach 45–49%, which is higher than GOS (10%–24%) [24].

Although many reviews have summarized research advances in HP scintillators, most have discussed their scintillation characteristics mainly from the perspectives of structural dimensionality, morphology, or crystal form [10, 42–44]. However, a systematic categorization of the primary methods for enhancing key scintillation parameters remains lacking. In this review, we initially clarify the fundamental working principle of x-ray detection. Then, we systematically analyze the main strategies for improving the performance of halide perovskite or perovskite-like scintillators, particularly in elevating light yield and shortening response-decay time. In addition, methods designed to control the direction of light transmission by chiral circularly polarized

TABLE 1 | Key parameters of the typical halide perovskite and other scintillation materials.

Materials type	Materials	ρ (g/cm^3)	Z$_{eff}$	Light yield (ph/MeV)	Decay time (ns)	Detection limit (nGy$_{air}$/s)	Spatial resolution (lp/mm)	Refs.
Halide Perovskites and their Derivatives	$CsPbBr_3$	——	——	——	44.6	13	——	[23]
	$CsPbBr_3$	——	——	177 000	200	——	9.8	[24]
	$Cs_2Ag_{0.6}Na_{0.4}In_{1-y}Bi_yCl_6$	——	——	39 000 ± 7 000	1.6×10^4	19	4.4	[25]
	$(EDBE)PbCl_4$	2.191	67.52	9 000	7.9	——	——	[18]
	$(TPA)_2MnBr_4$	——	——	56 800	1.25×10^4	18.7	21	[26]
	$BA_2PbBr_4{:}Mn^{2+}$	——	——	85 000	——	16	10.7	[27]
	$Cs_2AgI_3{:}Cu$	4.62	——	82 900	192.8	77.8	16.2	[28]
	Rb_2CuBr_3	3.83	34.99	91 056	4.14×10^4	121.56	——	[29]
	$Cs_3Cu_2I_5$	4.28	52.4	79 280	1.92×10^3	——	——	[30]
	Cs_2ZrCl_6	3.94	——	49 400	1.556×10^4	65	18	[31]
	Cs_2HfCl_6	3.9	57.6	21 700	——	55	11.2	[32]
Other Halides	$Cu_4I_6(L_1)_2$	——	——	32 600	5.58×10^3	96.4	>30	[33]
	$Cu_4I_6(L_2)_2$	——	——	30 500	2.33×10^3	102.1	>30	[33]
	Cs_3TbCl_6	3.55	43.07	56 800	5.23×10^6	149.65	3.3	[34]
	Rb_3TbCl_6	3.18	41.13	88 800	4.38×10^6	115.38	3.9	[34]
	$Cs_4CaI_6{:}Yb^{2+},Sm^{2+}$	——	——	52 000	——	186	——	[40]
	CsI:Tl	4.51	54	65 000	1000	180	10	[35]
	NaI:Tl	3.67	51	38 000	230	——	——	[36]
Oxides	BGO	7.13	74	85 000	300	376	11	[35]
	$PbWO_4$	8.28	75	400	10	——	——	[36]
	$CaMoO_4{:}Eu^{2+}$	——	——	——	6.7×10^5	76	23	[37]
Oxysulfide	GOS	7.34	61.1	66 000	1200	——	6.2	[24]
Fluoride	BaF_2	4.89	52.7	1 400	0.06	——	——	[36]
Organic materials	TPE-4Br (crystal)	——	35	34 600	1.79	——	——	[38]
	NE102 A (plastic)	1.03	5.7	1 000	2	——	——	[36]
	EHCZ (liquid)	1	——	6 000	20	——	——	[39]

*$Cu_4I_6(L_1)_2$, L_1 = 1-propyl-1,4-diazabicyclo[2.2.2]octan-1-ium; $Cu_4I_6(L_2)_2$, L_2 = 4-dimethylamino-1-ethyl-Pyridinium; TPE-4B, 1,1,2,2-tetrakis(4-bromophenyl) ethylene; EHCZ, N-(2-ethylhexyl)carbazole.

luminescence, waveguide effects, and enhancement of transparency are introduced to boost the spatial resolution of x-ray imaging. Finally, we emphasize the major challenges currently and offer insights into the further development and application of high-performance scintillators.

2 | Working Mechanism of X-ray Detection

The indirect detection process mainly involves three stages: the absorption and conversion of x-ray photons, the transport of charge carriers, and the luminescence resulting from radiative recombination [45]. The conversion stage involves the interaction between x-rays and the lattice atoms to generate electron-hole pairs. When the incident photon energy is within the range of 100 eV–100 keV, the photoelectric effect plays a major role. Outside this range, Compton scattering takes effect. As the incident radiation energy exceeds 1.02 MeV (equivalent to $2m_ec^2$, where m_e is the rest mass of the electron and c denotes the light velocity), the pair production mechanism becomes possible [46]. These electrons produce many secondary electrons through electron–electron scattering and Auger processes, thereby forming charge carriers. Subsequently, these charge carriers consume energy in the form of thermal energy through interaction with phonons and ultimately accumulate in the conduction band and valence band. In the second stage, the generated electrons and holes transport to the luminescent centers, completing the energy transfer process. During this process, carriers are susceptible to being trapped at various defects or self-trapped in the lattice, resulting in non-radiative energy dissipation and potential delay in radiative recombination. The luminescence stage is achieved by the radiative recombination of electrons and holes, releasing ultraviolet-visible light. Finally, the light is captured and measured by following photomultipliers or photodetectors (Scheme 2). It is

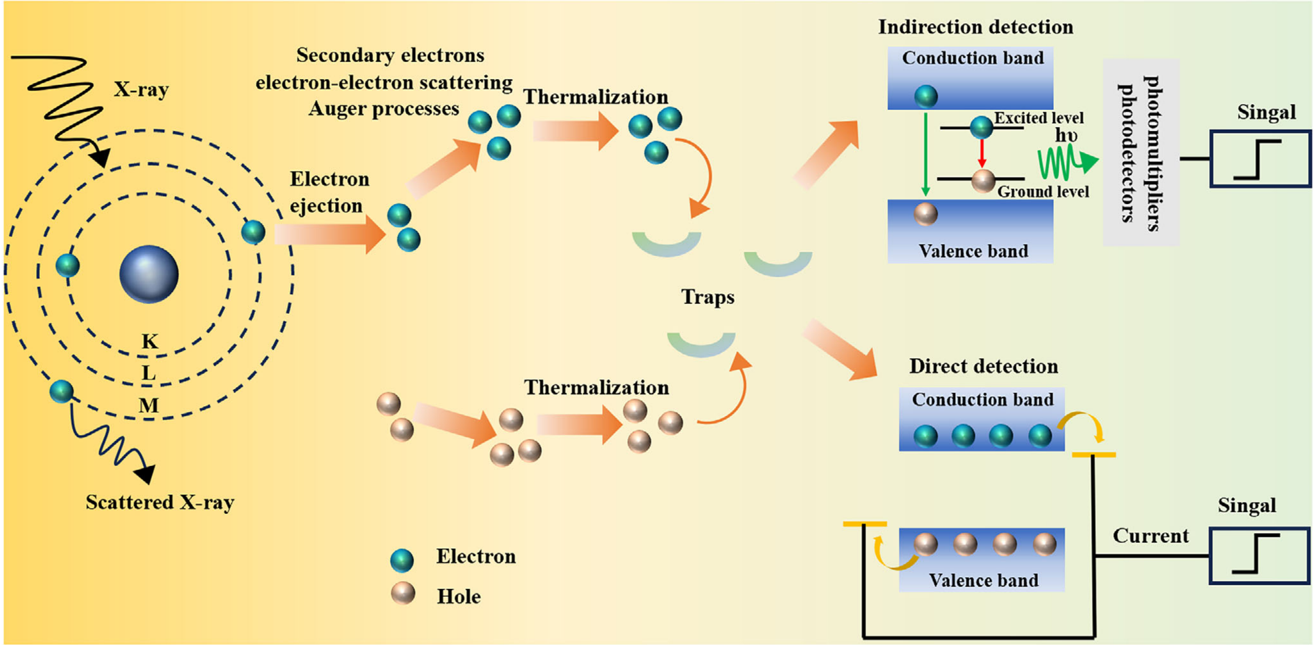

SCHEME 2 | Schematic illustration of x-ray detection.

important to recognize that the above mechanism is specific to inorganic scintillators. In the case of organic or non-crystalline scintillators, the mechanism may be more complex [47].

In direct detection, the conversion process is similar to that of indirect detection, where x-rays generate a substantial number of electron-hole pairs within the semiconductor. The fundamental distinction lies in the mechanism of electrical signal generation. Upon application of an electric field, electrons and holes migrate toward their opposite electrodes to generate a measurable current (Scheme 2). Direct x-ray detectors have two operating modes: current mode and pulse mode [48]. Current mode detectors record the average current value generated by particles and are suitable for receiving high-flux high-energy photons. Pulse mode detectors capture the voltage pulse corresponding to each particle and are typically employed under low-flux conditions, enabling the preservation of both energy and time information for individual radiation events.

3 | Strategies for Enhancing Performance of HP Scintillators

3.1 | Light Yield Improvement

Light yield (LY) is defined as the number of detectable photons produced per 1 MeV of absorbed energy (photons/MeV). It can be expressed as [36]:

$$\mathrm{LY} = 10^6 \mathrm{SQ}/\beta \mathrm{E}_g$$

where S and Q represent the efficiency of electron-hole pair transport to luminescent centers and their radiative recombination, respectively. β is typically taken as 2.5, and E_g is the bandgap of the scintillator. A high light yield is essential for high-sensitivity x-ray detection. Benefiting from their relatively narrow bandgaps of 1.5–3.2 eV, HP scintillators can theoretically achieve light yields of approximately 129 000–250 000 photons/MeV. In practice, however, the measured values are typically lower than the predicted ones [49]. This is attributed to factors such as self-absorption, non-radiative recombination, and light transport losses. To approach the theoretical upper limit, researchers have proposed several strategies and made notable progress in experiments. Here, four main methods are summarized: enhancing exciton binding energy, expanding Stokes shift, constructing HP composite materials, and improving material crystallinity.

3.1.1 | Increasing Exciton Binding Energy

The light yield is affected by the exciton binding energy (E_b), which refers to the energy needed to separate a bound electron-hole pair into free carriers. A higher exciton binding energy signifies greater exciton stability, reducing the likelihood of dissociation. During the recombination process, a large amount of energy is released, which facilitates the generation of more photons and an increase in light yield. At present, the exciton binding energy can be enhanced by reducing the structural dimension and crystal size.

3.1.1.1 | Reduction in Structural Dimension. Two-dimensional (2D) HPs are composed of alternating organic ligands and inorganic perovskite layers. The organic layers possess a higher energy gap and function as barriers, whereas the inorganic layers, with a lower energy gap, form potential wells, thereby creating a quantum well structure [50]. Although the incorporation of organic ligands reduced the overall material ρ and Z_{eff}, the unique low-dimensional architecture spatially confines excitons within the inorganic layers. This quantum confinement increases the overlap between electron and hole wavefunctions and intensifies the Coulomb interaction [42],

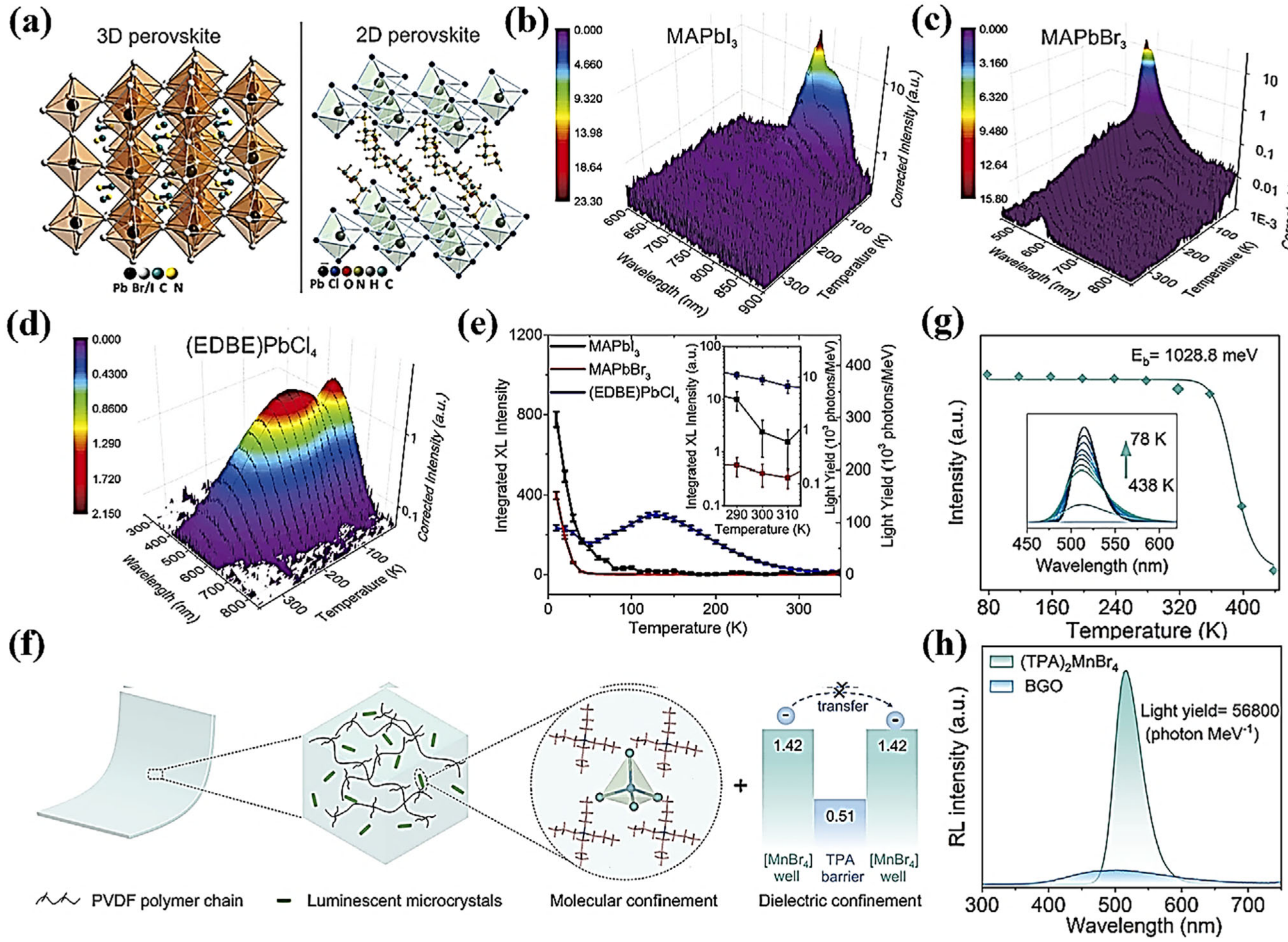

FIGURE 1 | (a) Crystal structure representation of $MAPbX_3$ (X = I, Br) (left), and $(EDBE)PbCl_4$ (right). Radioluminescence (RL) spectra of perovskite crystals at various temperatures from 10 to 350K: (b) $MAPbI_3$, (c) $MAPbBr_3$, and (d) $(EDBE)PbCl_4$. (e) Light yields of $MAPbI_3$, $MAPbBr_3$, and $(EDBE)PbCl_4$ obtained from the integrated x-ray excited luminescence intensities at various temperatures from 10–350K. Reproduced with permission [18]. Copyright 2016, Springer Nature. (f) Demonstration of molecular and dielectric confinement. (g) Integral PL intensities of $(TPA)_2MnBr_4$ versus temperature. The inset shows the temperature-dependent PL spectra of $(TPA)_2MnBr_4$. (h) RL spectra of $(TPA)_2MnBr$ and BGO (tube voltage: 50 kV, beam current: 80 µA, dose rate: 278 μGy_{air}/s). Reproduced with permission [26]. Copyright 2025, Wiley-VCH.

ultimately enhancing the exciton binding energy in 2D HPs with higher light yield.

In 2016, Soci et al. compared the x-ray scintillation properties of three-dimensional (3D) perovskites $MAPbI_3$ and $MAPbBr_3$ (MA = CH_3NH_3) as well as 2D perovskite $(EDBE)PbCl_4$ (Figure 1a) [18]. All perovskite single crystals (SCs) demonstrated high x-ray scintillation efficiency at low temperatures (Figure 1b–d). At a temperature of 130 K, the light yield of $(EDBE)PbCl_4$ could reach approximately 120 000 photons/MeV, while $MAPbI_3$ and $MAPbBr_3$ exceeded 150 000 photons/MeV only at 10K. Due to pronounced thermal quenching effects, the light yields of 3D perovskites dropped sharply at room temperature (<1000 photons/MeV). In contrast, by designing the structure and dimension of perovskites, the $(EDBE)PbCl_4$ crystal, with a large exciton binding energy (about 360 meV), was less affected by thermal quenching (~9 000 photons/MeV under the same condition) (Figure 1e). Liu et al. developed an airflow-controlled solvent evaporation method to successfully grow $(PEA)_2PbBr_4$ SCs with a diameter exceeding two inches [51]. The crystal structure features alternating inorganic $[PbBr_4]^{2-}$octahedral layers and organic PEA^+ cation layers, where two organic layers sandwich one inorganic layer, and adjacent layers are held together by weak van der Waals interactions. Owing to the synergy of organic and inorganic components, the $(PEA)_2PbBr_4$ SCs exhibited a high light yield of 73 226 photons/MeV and a fast response time of 14 ns. Besides, lower-dimensional perovskites (1D and 0D) also manifest high exciton binding energies. For example, a hybrid scintillator $(TPA)_2MnBr_4$ with strong bound exciton behavior is constructed by leveraging the effects of molecular and dielectric confinement (Figure 1f), achieving an exciton binding energy of 1028.8 meV (Figure 1g) [26]. Under x-ray irradiation, $(TPA)_2MnBr_4$ accomplished a light yield of up to 56 800 photons/MeV (Figure 1h).

3.1.1.2 | HP Nanocrystals or Quantum Dots.

3D perovskites reveal small exciton binding energy because of high dielectric constant and poor quantum confinement, dramatically lowering light yield at room temperature compared to low-temperature conditions. Reducing the size of 3D HPs from SCs to nanocrystals (NCs) or quantum dots (QDs) can strengthen exciton binding energy through spatial confinement.

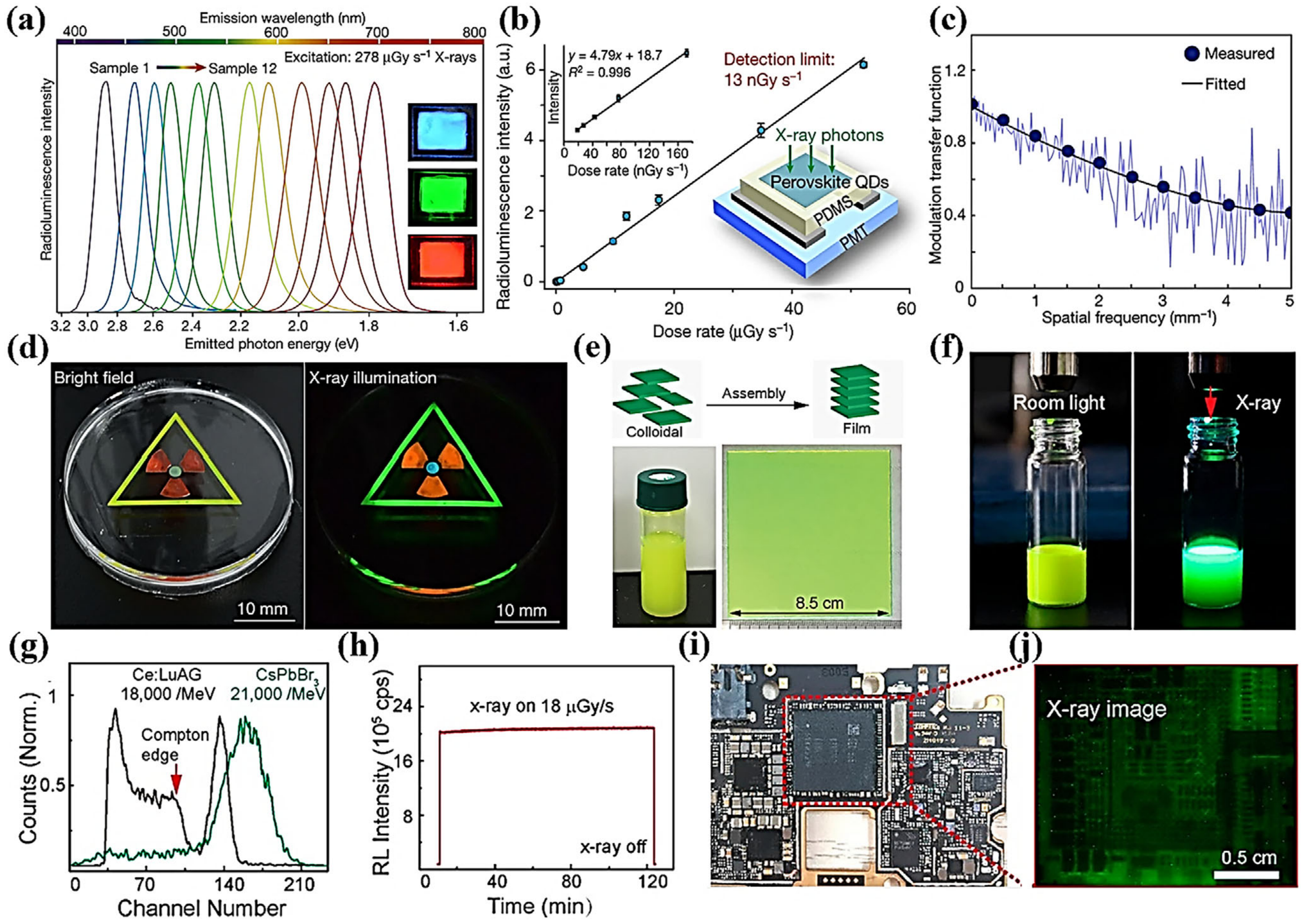

FIGURE 2 | (a) Tunable emission spectra of perovskite QDs under x-ray illumination. (b) RL measurements for $CsPbBr_3$ NCs-based scintillator as a function of dose rate. (c) Spatial resolution of the x-ray imaging system under 15 μGy of x-ray exposure. (d) Multicolor visualization of perovskite QD scintillators (left, bright-field imaging; right, x-ray illumination at a voltage of 50 kV). Reproduced with permission [23]. Copyright 2018, Nature Publishing Group. (e) Schematic depiction of the self-assembly process of $CsPbBr_3$ nanosheets. (f) Photographs of the concentrated colloids under ambient light and x-ray irradiation. (g) Pulse height spectra of a standard commercial scintillator (Ce:LuAG) and a $CsPbBr_3$ colloid scintillator. (h) Intensity record of the thin-film RL over 2 h exposure of x-ray radiation with 18 $\mu Gy_{air}/s$. (i) Photograph of a transistor panel in a cellphone. (j) X-ray imaging of the interior structure of the resin-covered panel (red dashed square) by the perovskite thin-film screen. Reproduced with permission [52]. Copyright 2019, American Chemical Society.

In 2017, an initial investigation into the impact of x-ray irradiation on the radioluminescence of $CsPbBr_3$ QDs was reported [53]. It has been demonstrated that x-rays can directly interact with $CsPbBr_3$ QDs, highlighting their potential as a promising scintillation material. Subsequently, Liu et al. investigated the multicolor x-ray scintillation phenomenon of a series of all-inorganic $CsPbX_3$ (X = Cl, Br, I) NCs [23]. Unlike traditional scintillators, these scintillators can flexibly tune the radiation luminescence within the visible spectrum range by adjusting the anionic composition of colloidal precursors (Figure 2a). The $CsPbBr_3$-based scintillator achieved a detection threshold as low as 13 nGy_{air}/s (Figure 2b) and a very short decay time ($\tau_{decay} = 44.6$ ns). The modulation transfer function (MTF) of this perovskite NCs-based x-ray detector reached 0.72 at a spatial resolution of 2.0 lp/mm (Figure 2c), which outperforms commercial CsI:Tl flat-panel x-ray detectors (0.36 at 2.0 lp/mm). Moreover, the study exhibited that these color-tunable perovskite quantum dot scintillators can serve as convenient visualization tools in x-ray photography (Figure 2d). Xu et al. embedded $CsPbBr_3{:}Lu^{3+}$ NCs into a transparent amorphous matrix to prepare a scintillator with exceptional x-ray radiation resistance [54]. The introduction of Lu^{3+} promoted the uniform distribution of $CsPbBr_3$ NCs in the matrix, enabling a high imaging resolution (about 16.8 lp/mm) and a low detection dose (50 nGy_{air}/s). Interestingly, the performance degradation caused by x-ray irradiation could be effectively restored through simple thermal annealing, which was attributed to the high-viscosity amorphous network structure confining the perovskite NCs in a local environment. This characteristic offers good recyclability in practical applications. To address the challenge of forming perovskite nanocrystal scintillator films with controlled thickness and large-area size, a room-temperature synthesis for colloidal $CsPbBr_3$ nanosheet-based scintillators has been reported (Figure 2e,f) [52]. The light yield of the colloidal scintillator achieved 21 000 photons/MeV, which exceeds the commercial Ce:LuAG single-crystal scintillator (18 000 photons/MeV) (Figure 2g). Notably, this scintillator was easy to process and could be fabricated into large-area, uniform, and crack-free films (8.5 × 8.5 cm^2 in area), exhibiting long-term stability under continuous x-ray irradiation (Figure 2h) and high-resolution x-ray imaging performance (Figure 2i,j).

TABLE 2 | Recent published works on ion-doped halide perovskites for scintillation performance.

Materials type	Materials	Emission wavelength (nm)	Stokes shift (nm)	Light yield (ph/MeV)	Decay time (μs)	Spatial resolution (lp/mm)	Detection limit (nGy$_{air}$/s)	Refs.
Mn-based doped halide perovskite scintillators	$CsMnCl_3$	650	285	13 400	370.3	4	470×10^3	[56]
	$Cs_2NaLuCl_6$:Mn^{2+}	628	308	——	10.79×10^3	20	0.99×10^3	[57]
	$Cs_2CdBr_2Cl_2$:Mn^{2+}	495/593	210/308	64 950	70.74	12.3	17.82	[58]
	Cs_2CdCl_4:Mn^{2+}	585	340	88 183	24.3×10^3	16.1	31.04	[59]
	BA_2PbBr_4:Mn^{2+}	610	222	85 000	727.83	10.7	16	[27]
	DA_2PbBr_4:Mn^{2+}	620	255	35 292	739.4	10	108.17×10^3	[60]
	$[TPPen]_2MnBr_4$	515	65	43 000	298.04	4.6	696.9	[61]
	$Cs_3Cu_2I_5$:Mn^{2+}	565	185	65 000	——	11.8	49	[62]
	Cs_3ZnBr_4:Mn^{2+}	526/655	161/290	15 600	255.90 /163.63	5.06	1.16×10^3	[63]
Lanthanide-doped halide perovskite scintillators	$CsPbBr_3$:Eu^{3+}	530/613	165/248	10 100	6.78×10^{-3}	15	——	[64]
	$CsPbCl_3$:Yb^{3+}	980	>550	112 000	1.242×10^3	——	176.5	[55]
	$CsNaTbCl_6$:Ce^{3+}	548	206	52 153	5.71×10^3	10	30	[65]
	Cs_4SrI_6:Eu^{2+}	474	97	62 300	1.9	——	——	[66]
	Cs_4CaI_6:Eu^{2+}	474	97	51 800	2.1	——	——	[66]

*[Tppen]2MnBr4, Tppen = pentyltriphenylphosphonium

3.1.2 | Expanding Stokes Shift

To ensure efficient x-rays absorption, scintillator materials need to have a certain thickness, which unfortunately exacerbates the self-absorption effect. This issue is prominent in HP materials due to their small Stokes shift, reducing the overall light yield. Expanding the Stokes shift is a primary approach to mitigate the self-absorption phenomenon. Researchers have tackled the problem by doping with transition metal ions or lanthanide ions, as well as harnessing self-trapped exciton (STE) emission.

3.1.2.1 | Ion Doping. Transition metal ions (e.g., Mn^{2+}, Cu^{2+}) and lanthanide ions (e.g., Eu^{3+}, Tb^{3+}) have abundant electronic transition energy levels, which allow for light emission at specific wavelengths. Introducing these ions into the HP structure not only can serve as new luminescent centers through energy transfer (ET) of the host matrix, but also regulates the band structure of materials, expanding the Stokes shift. Table 2 summarizes the main performance of recently reported ion-doped HP scintillators [27, 55–66].

A set of BA_2PbBr_4 perovskites with different Mn^{2+} doping concentrations were developed for scintillation applications [27]. As an activator, the incorporation of Mn^{2+} induces a large Stokes shift, nearly eliminating self-absorption effects (Figure 3a,b). At a Mn^{2+} doping concentration of 10%, the scintillator delivered 85 000 photons/MeV in light yield (Figure 3c), accompanied by a detection limit as low as 16 nGy$_{air}$/s (Figure 3d). Additionally, the researchers prepared a BA_2PbBr_4:10%Mn^{2+}-PMMA composite scintillation screen, achieving high-resolution x-ray imaging of both planar and non-planar objects (Figure 3e). Han et al. doped Mn^{2+} into all-inorganic 2D Cs_2CdCl_4 perovskite SCs, obtaining bright orange-red luminescence through effective energy transfer from the Cs_2CdCl_4 host matrix to the Mn^{2+} dopant ions [59]. As a scintillator, Cs_2CdCl_4:10% Mn had high light yield (88138 photons/MeV), and excellent thermal quenching resistance. Song et al. pioneered the quantum-cutting (QC) scintillators based on $CsPbCl_xBr_{3-x}$:Yb^{3+} SCs [55]. By leveraging ET from $CsPbCl_xBr_{3-x}$ to Yb^{3+}, a QC effect was achieved, attaining a PLQY of 149% and a Stokes shift exceeding 550 nm (Figure 3f,g). The scintillator displayed high transmittance, negligible self-absorption, and large x-ray conversion efficiency, achieving high light yield (112 000 photons/MeV) (Figure 3h) and a low detection limit (176.5 nGy$_{air}$/s) (Figure 3i).

3.1.2.2 | Emissions of Self-trapping Excitons. In HPs, excitons have strong coupling with lattice phonons, leading to energy dissipation through lattice vibrations and the formation of localized lattice distortions. These distortions create a potential well that confines the excitons, forming a self-trapped exciton (STE) state. Subsequently, the STEs undergo radiative recombination to the ground state, holding characteristic large Stokes shifts and broad emission spectra. Low-dimensional halide perovskite-like structures are more prone to form STE due to their soft lattice nature and pronounced exciton-phonon interaction [67].

A novel lead-free halide perovskite-like scintillator, Rb_2CuBr_3 (Figure 4a), whose 1D crystal structure and soft lattice properties are conducive to the generation of STEs (Figure 4b) [29]. During the excitation process, the electronic configuration of $Cu^+(3d^{10})$ transformed into $Cu^{2+}(3d^9)$, triggering Jahn–Teller distortion. Based on these advantages, Rb_2CuBr_3 obtained a Stokes shift of 85 nm with almost no overlap between the PL and absorption spectra (Figure 4c), realizing a record-breaking light yield of 91 056 photons/MeV (Figure 4d). A flexible and large-area x-ray scintillation screen based on Cu-doped Cs_2AgI_3 polycrystalline powders was reported [28]. The PLE and PL peaks of Cs_2AgI_3:Cu appeared at 304 and 470 nm, respectively, showing an

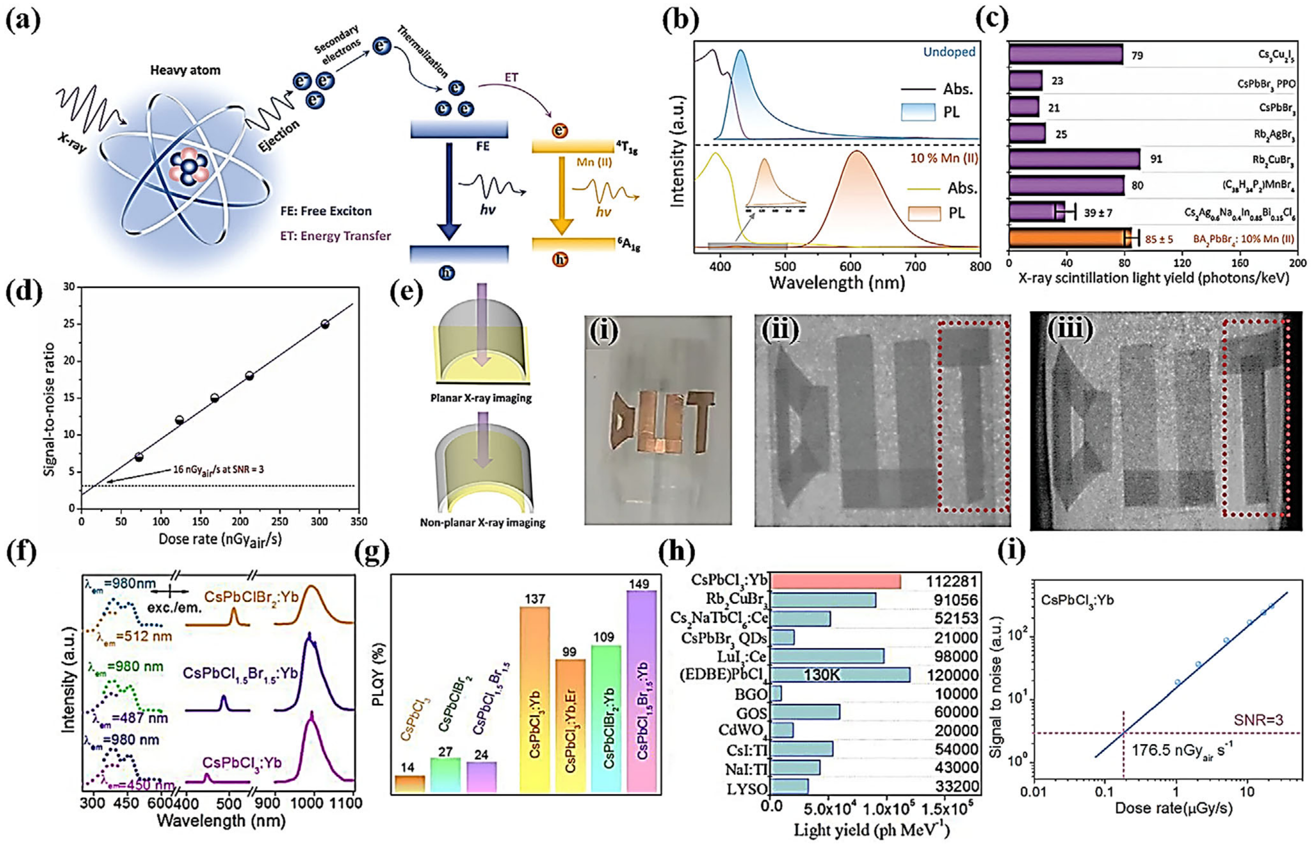

FIGURE 3 | (a) Proposed mechanism of x-ray scintillation in BA_2PbBr_4:Mn^{2+}. (b) Absorption and PL spectra of undoped (top) and 10% Mn^{2+} doped (bottom) BA_2PbBr_4 perovskites. (c) Comparison of light yields of BA_2PbBr_4:10% Mn^{2+} with several reported perovskite scintillators. (d) Signal-to-noise ratio (SNR) as a function of x-ray dose rate on BA_2PbBr_4:10% Mn^{2+}-PMMA. (e) Plot of planar and nonplanar x-ray imaging. (i) Photograph, (ii) planar image, and (iii) nonplanar image of copper tape with DUT pattern glued to a bent plastic sheet. Reproduced with permission [27]. Copyright 2022, Wiley-VCH. (f) PL excitation (PLE) (left) and PL (right) spectra of $CsPbCl_xBr_{3-x}$:Yb^{3+} SCs. (g) PLQY values of $CsPbCl_xBr_{3-x}$ SCs with/without lanthanide ions doping. (h) Comparison of light yields between $CsPbCl_3$:Yb^{3+} SCs and several typical scintillators. (i) X-ray dose rate-dependent SNR for $CsPbCl_3$:Yb^{3+} SCs. Reproduced with permission [55]. Copyright 2023, Wiley-VCH.

ultra-broad PL spectrum with a full width at half maximum (FWHM) of 135 nm (Figure 4e). As shown in Figure 4f, the light yield reached 82 900 photons/MeV, which is comparable to that of Rb_2CuBr_3. Besides low-dimensional perovskite derivatives, double perovskites also exhibit typical STE luminescence. Yang et al. synthesized a series of nontoxic double perovskite scintillators, $Cs_2Ag_{0.6}Na_{0.4}In_{1-y}BiCl_6$ [25]. By doping Na^+ into $Cs_2AgInCl_6$, the parity-forbidden transition was partially broken, promoting radiative recombination of STEs and achieving intense near-white light emission. The doping of Bi^{3+} not only enhanced the x-ray stopping power of $Cs_2Ag_{0.6}Na_{0.4}InCl_6$ but also tuned the luminescent characteristics of double perovskites. Thanks to the large Stokes shift between the PL and absorption spectra brought by STEs (Figure 4g), the light yield of the $Cs_2Ag_{0.6}Na_{0.4}In_{0.85}Bi_{0.15}Cl_6$ scintillator reached as high as 39 000 ± 7 000 photons/MeV (Figure 4h), enabling static and dynamic x-ray imaging at low doses without afterglow (Figure 4i,j). $Cs_2NaGdCl_6$ SCs showed a blue STE emission at 470 nm when excited at 265 nm. Lee et al. added Tb^{3+} to this basis and achieved green emission at 549 nm via ET from STE to Tb^{3+} [68]. Consequently, $Cs_2NaGdCl_6$:Tb^{3+} scintillation films delivered excellent imaging quality, offering a light yield of 39 100 ph/MeV and an x-ray detection threshold down to 41.32 nGy_{air}/s.

3.1.3 | Constructing HP Composite Materials

In HP composite materials, ET channels are established via the cooperative interaction of constituent materials. Such structures benefit the directional transfer of excited-state energy to other components with matched energy levels, boosting energy conversion efficiency. Brovelli et al. engineered $CsPbBr_3$ NCs as sensitizers for a conjugated organic emitter to attain a plastic scintillator (Figure 5a,b) [69]. The absorption spectrum of this organic emitter perfectly overlapped with the emission of $CsPbBr_3$ NCs (Figure 5c). Under x-ray irradiation, the energy from the NCs was entirely transferred to the organic dye, achieving a light yield of 9 000 photons/MeV. An ET strategy from $CsPbBr_3$ nanowires to pyrromethene 597 (PM597) was devised by Hu et al. (Figure 5d) [70]. Compared with $CsPbBr_3$ nanowires, the emission of $CsPbBr_3$ nanowires/PM597 showed a substantial Stokes shift, avoiding the self-absorption phenomenon of perovskites (Figure 5e). This ET process enhanced the performance of the scintillator, achieving a low detection limit of 152 nGy_{air}/s (Figure 5f), a spatial resolution of 11.5 lp/mm (Figure 5g), and a light yield of 15 600 photons/MeV, which is 4.1 times higher than that of pure perovskite nanowire scintillators.

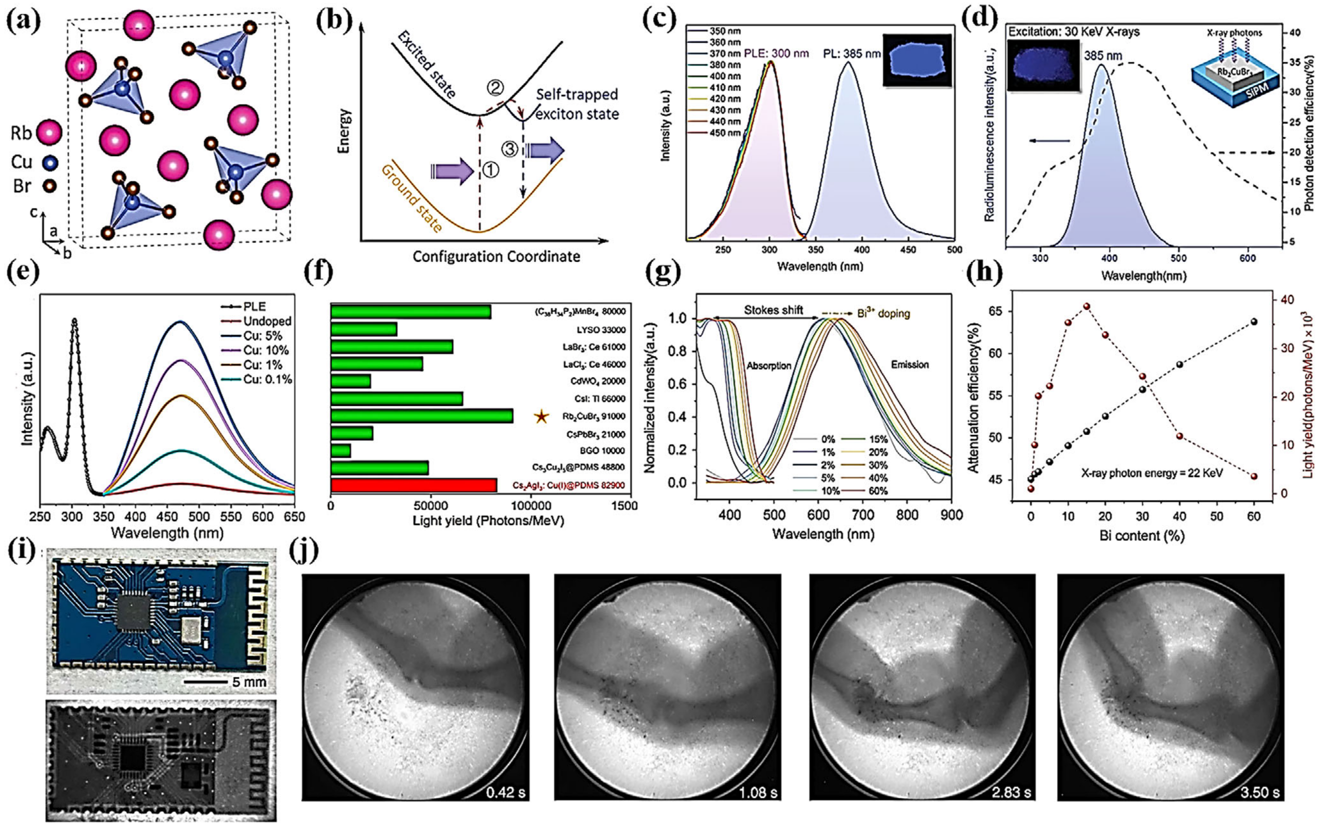

FIGURE 4 | (a) Crystal structure of Rb_2CuBr_3. (b) Schematic diagram of STE luminescence mechanism. (c) PL spectrum of Rb_2CuBr_3 excited by 300 nm and PLE spectra measured at different emission wavelengths from 350 to 450 nm. (d) RL spectrum under 30 keV x-ray excitation and wavelength-dependent photon detection efficiency of the silicon photomultiplier. Reproduced with permission [29]. Copyright 2019, Wiley-VCH. (e) PLE and PL spectra of Cs_2AgI_3:Cu powders. (f) Comparison of light yields between Cs_2AgI_3:Cu@PDMS and commercially available scintillators. Reproduced with permission [28]. Copyright 2022, American Chemical Society. (g) Stokes shift of $Cs_2Ag_{0.6}Na_{0.4}In_{1\text{-}y}BiyCl_6$ with different Bi^{3+} contents. (h) Attenuation efficiency and light yield of $Cs_2Ag_{0.6}Na_{0.4}In_{1\text{-}y}BiyCl_6$ versus Bi^{3+} content. (i) Photograph of a circuit board (top) and its x-ray image (below). (j) Real-time x-ray images of finger bending. (dose rate:47.2 μGy_{air}/s, voltage:50 kV). Reproduced with permission [25]. Copyright 2020, Springer Nature.

3.1.4 | Increasing the Crystallinity of Materials

Materials with low crystallinity usually contain a higher density of defects, which can trap excitons and thereby affect detection sensitivity. Increasing the crystallinity of materials makes more ordered atomic arrangements. This well-ordered structure can minimize scattering losses, promoting the efficiency of electron transitions [71]. Therefore, enhancing crystallinity is also a viable way to increase the x-ray light yield.

Xiang et al. successfully precipitated $CsPbBr_3$:Eu^{3+} NCs by thermal treatment. The incorporation of Eu^{3+} promotes the nucleation of NCs and a more uniform distribution of $CsPbBr_3$ within the glass (Figure 6a,b), attenuating light scattering and acquiring clear x-ray images (Figure 6c) [72]. An ultrasonic-assisted crystallization integrated with the hot-pressing method was proposed to construct high-quality quasi-monocrystalline $MA_{0.42}FA_{0.58}PbI_3$ thick films (Figure 6d) [73]. The rapid ultrasonic-assisted crystallization facilitates more uniform nucleation, and the subsequent hot-pressing treatment allows for grains rearrangement (Figure 6e), eliminating the voids between crystals and further optimizing the crystallinity. This x-ray detector manifested an exceptionally high sensitivity (1.16×10^6 μC/Gy_{air} cm^2) (Figure 6f) and a low detection limit (37.4 nGy_{air}/s) (Figure 6g), making it one of the top-performing perovskite-based x-ray detectors reported so far. The inch-sized $(PEA)_2PbBr_4$ SCs were prepared by evaporation crystallization coupled with nucleation control (Figure 6h) [74]. The crystals were placed under a constant temperature and humidity atmosphere to obtain superior crystal dimensions and quality, addressing the problem of heterogeneous crystallization in organic–inorganic perovskites. The crystals exhibited a photon yield of 38 600 photons/MeV and a spatial resolution as high as 23.2 lp/mm (MTF = 20%) (Figure 6i), gaining high-performance large-area imaging (Figure 6j).

3.2 | Fast Response-Decay Time

Response time refers to the speed at which a scintillator converts absorbed x-rays into ultraviolet/visible light emission. Scintillators with fast response are essential for strengthening the clarity and dynamic range of imaging. In practical applications, luminescence decay time means the interval taken for a scintillator's emitted light signal to drop from its peak intensity to approximately 1/e of the original value. A short decay time denotes the scintillator can return to its initial state more quickly, avoiding signal overlap and pile up.

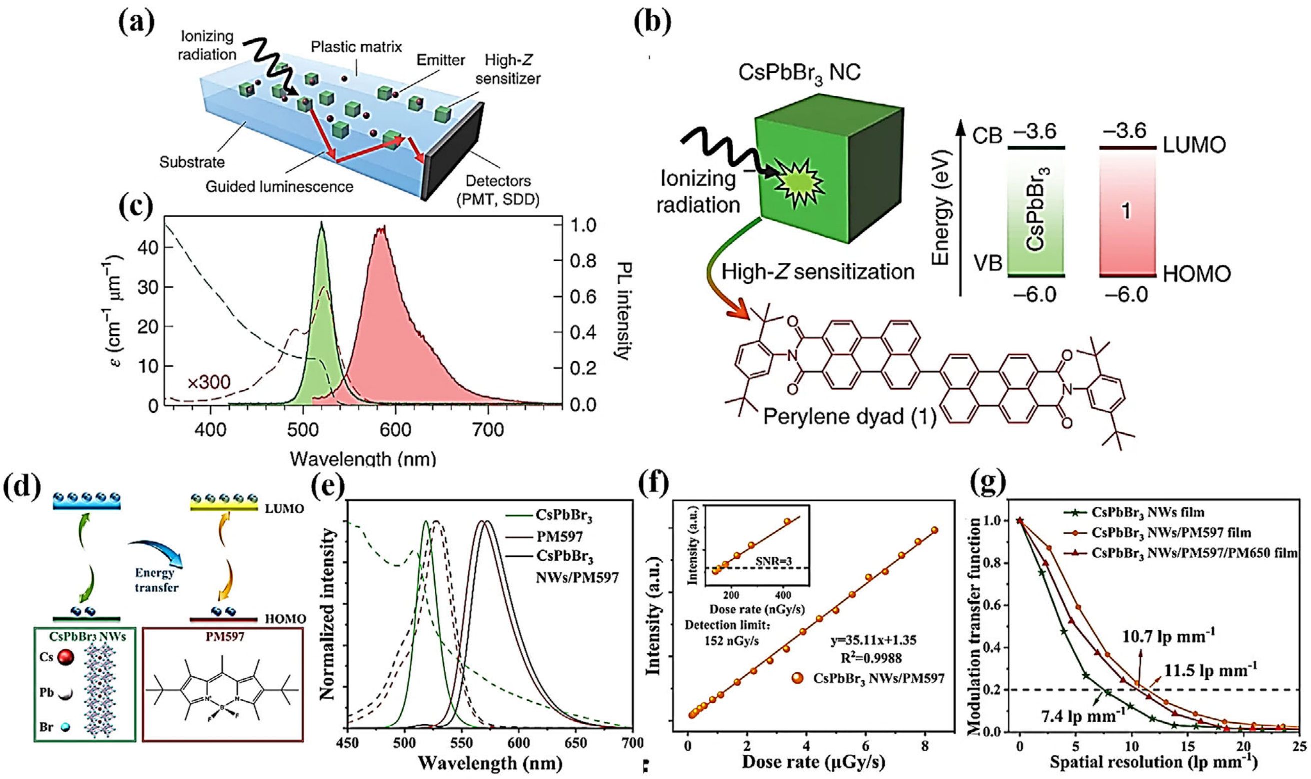

FIGURE 5 | (a) Schematic depiction of a sensitized plastic scintillator. (b) Sketch of $CsPbBr_3$ NCs sensitizing the organic emitter. (c) Molar extinction coefficient (dashed lines) and PL spectra (solid lines) of NCs (green, $\lambda_{ex} = 405$ nm) and organic emitter (red, $\lambda_{ex} = 500$ nm). Reproduced with permission [69]. Copyright 2020, Nature Publishing Group. (d) Diagram of ET between the $CsPbBr_3$ nanowires and PM597. (e) The absorption (dashed lines) and PL (solid lines) spectra of $CsPbBr_3$ nanowires, PM597, and $CsPbBr_3$ nanowires/PM597. (f) RL intensity of $CsPbBr_3$ nanowires/PM597 composite films at different x-ray doses. (g) MTF of $CsPbBr_3$ nanowires/PM597 composite films. Reproduced with permission [70]. Copyright 2024, American Chemical Society.

Scintillators with rapid response and brief decay duration have become a core driving force for the advancement of complex imaging techniques. For instance, in positron emission tomography (PET), the swift response can enhance the spatiotemporal resolution of images, thereby facilitating the precise control over the spatial distribution and concentration levels of radioactive tracers. In dynamic real-time x-ray imaging, the fast decay can capture the dynamic changes in rapidly moving organs or tissues, which is irreplaceable for the diagnosis and treating cardiovascular and respiratory diseases. Currently, researchers have found that quick response features are more common in lead-based halide perovskite materials (Table 3) [18, 23, 29, 51, 75–92]. There are numerous shallow-level defects in both the interior and surface of 3D lead-based perovskites, causing decay times typically in the order of nanoseconds. The luminescence mechanism mainly originates from free carrier recombination [93]. In contrast, the multiple quantum well structures of 2D perovskites can localize excitons within the inorganic layers, with the primary emission mechanism being exciton recombination [94]. These structures intensify radiative recombination efficiency, potentially giving rise to short decay times, and the exact value varies depending on the specific material and structure. In low-dimensional perovskites, strong electron-lattice coupling tends to induce the formation of STEs [95]. As a result, the lifetimes generally range from microseconds to milliseconds, making them unsuitable for optoelectronic devices with fast response on the nanosecond scale.

3.2.1 | 3D Lead-based HPs

A continuous $[PbX_6]^{4-}$ octahedral network of 3D lead-based perovskite equips it with high carrier mobility and provides an efficient charge transport channel. Meanwhile, its low exciton binding energy makes excitons easily dissociate into free carriers at room temperature, mainly via band-edge recombination luminescence. This luminescence mechanism leads to a faster luminescence decay time.

Unlike CsI:Tl scintillators with afterglow luminescence, the solution-processable $CsPbBr_3$ NC scintillator showed a very fast scintillation decay time ($\tau_{decay} = 44.6$ ns) when excited by pulsed photons from a portable ^{137}Cs source (661 keV), making it an ideal choice for dynamic real-time x-ray imaging [23]. Similarly, the $CsPbCl_3$ NCs treated with $CdCl_2$ eliminated deep hole traps caused by surface undercoordinated Cl^- via the cation exchange from Pb^{2+} to Cd^{2+}. This modification resulted in intense radiative emission and ultrafast radiative decay, with an average lifetime of as short as 210 ps and no observable defect-related slow emission tail [80]. The research team led by Ouyang et al. detected that small Br-doped $MAPbBr_{0.05}Cl_{2.95}$ SCs could boost scintillation performance [76]. The $MAPbBr_{0.05}Cl_{2.95}$ SCs showed a decay time of 0.14 ± 0.02 ns, which is attributed to the formation of a crystal structure with reduced defect density when partial Cl^- is replaced by Br^-, providing a purer bandgap and enhancing rapid, near-band-edge radiative recombination.

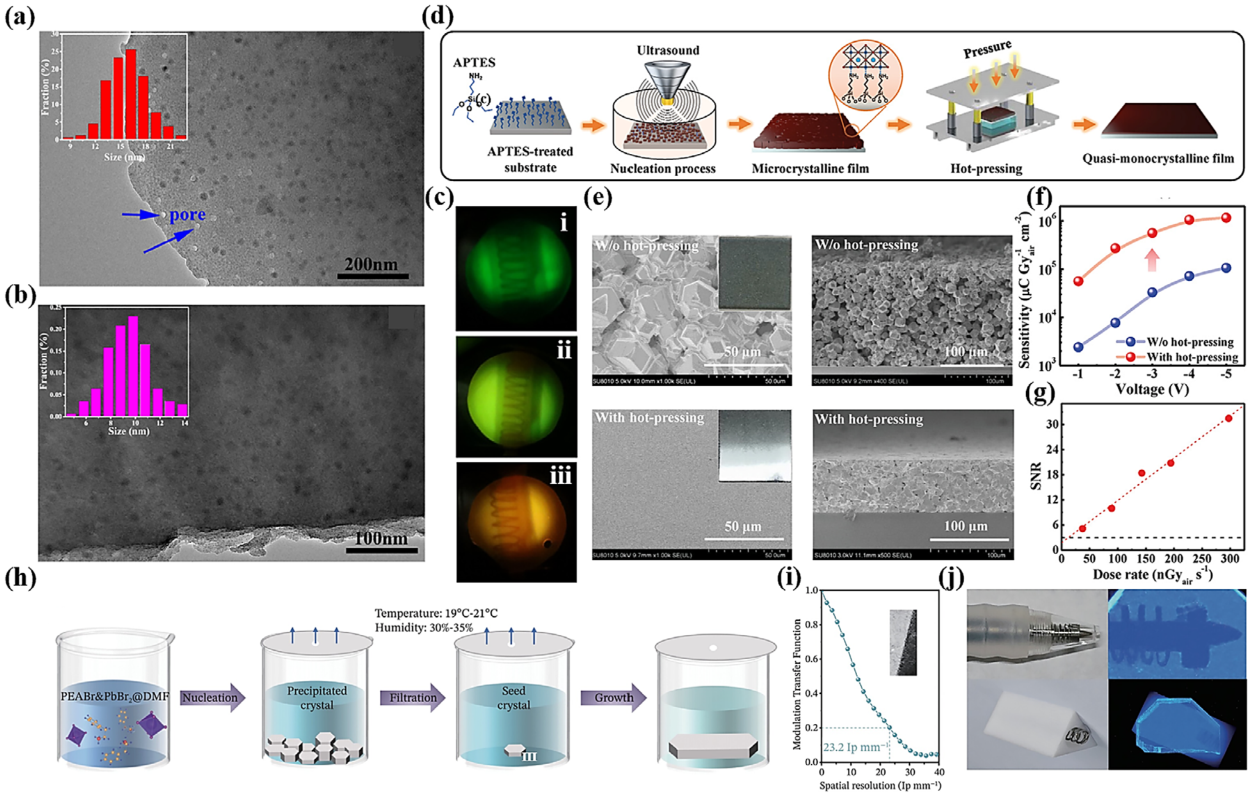

FIGURE 6 | TEM images and size distribution histograms of (a) $CsPbBr_3$-0Eu and (b) $CsPbBr_3$-1.8Eu. (c) x-ray images of (i) $CsPbBr_3$ -0Eu, (ii) $CsPbBr_3$-0.6Eu, and (iii) $CsPbBr_3$-1.8Eu. Reproduced with permission [72]. Copyright 2021, Chinese Laser Press. (d) Schematic illustration of the procedure for preparing a quasi-monocrystalline film. (e) SEM images (top) and cross-sectional SEM images (bottom) of the $MA_{0.42}FA_{0.58}PbI_3$ films with/without hot-pressing. (f) Sensitivities of devices based on $MA_{0.42}FA_{0.58}PbI_3$ films with/without hot-pressing. (g) SNR of the $MA_{0.42}FA_{0.58}PbI_3$ films-device under low dose rates. Reproduced with permission [73]. Copyright 2023, Wiley-VCH. (h) Schematic diagram of evaporation crystallization combined with a nucleation-controlled process for $(PEA)_2PbBr_4$ SCs growth. (i) MTF curves for the $(PEA)_2PbBr_4$ SCs. (j) Photographs and x-ray images of a ballpoint pen and a spring encapsulated in a polytetrafluoroethylene triangular prism. Reproduced with permission [74]. Copyright 2024, Wiley-VCH.

3.2.2 | 2D Lead-based HPs

Owing to a quantum confinement effect enlarging the overlap region of electron and hole wavefunctions, the scintillation of $(n\text{-}C_mH_{2m+1}NH_3)_2PbX_4$ (m = 3, 4, 6, 10, etc.), abbreviated with C_mPbX_4, had extremely short lifetimes [83]. The radiative recombination time of free excitons for C_3PbBr_4 was 2.8 ns, comparable to that of organic scintillators. The C_6PbI_4 crystal, on the other hand, displayed an even shorter decay time of only 390 ps. In 2023, Niu et al. inserted benzimidazole (BM) between $[PbBr_6]^{2-}$ layers as the A-site in 2D perovskites (Figure 7a) [84]. The incorporation of benzimidazole reduced the polarity and dipole moment of organic molecules, thereby decreasing the dielectric permittivity. This structural modification maximized the permittivity difference between the organic barrier layer and inorganic well layer, benefiting the confinement of electron-hole pairs and accelerating the scintillation decay time (Figure 7b,c). The average lifetime of BM_2PbBr_4 was 0.95 ns, which is the shortest among all perovskite materials. Additionally, its light yield (3190 photons/MeV) was much higher than the traditional scintillators BaF_2 (1500 photons/MeV). With its rapid decay time and high light yield, BM_2PbBr_4 is considered as a promising option for a range of ultrafast detection applications. For instance, the measured coincidence time resolution (CTR) of a PET camera based on BM_2PbBr_4 is 207 ± 2.2 ps, even better than the commercial PET scintillator LYSO (experimental value 250 ± 3.1 ps).

3.3 | Control of Light Transmission

Scintillators usually exhibit isotropic radiative luminescence, implying that photons undergo multiple scattering during propagation. This causes interference among light signals across adjacent pixels, resulting in image blurring and resolution degradation [96–98]. This phenomenon of light scattering and crosstalk is particularly prominent in thick scintillator films. In addition, crystal boundaries and defects within the material further increase the probability of light scattering and exacerbate the crosstalk problem. To address this issue, potential strategies including chiral circularly polarized luminescence, waveguide effect, and improvement in material transparency can be implemented to better control the propagation direction of emitted photons.

3.3.1 | Chiral Circularly Polarized Luminescence

At present, the widely used scintillators are primarily composed of non-chiral structures, which typically have centrosymmetric

TABLE 3 | Summary of decay times in lead-based and lead-free halide perovskites.

Type	Materials	Dimension	Decay time (ns)	Refs.
Lead-based halide perovskites	$MAPbBr_{0.05}Cl_{2.95}$ SC	3D	0.14 ± 0.02	[76]
	$CsPbCl_3$ SC	3D	fast components:0.39 slow components: 7	[77]
	$CsPbCl_3$:La, Ag SC	3D	fast components:0.49 slow components: 7.2	[77]
	$MAPbCl_3$ SC	3D	5.85	[78]
	$CsPbBr_3$ SC	3D	1 ns at 7K	[79]
	$CsPbBr_3$ NC	3D	44.6	[23]
	$CsPbCl_3:CdCl_2$ NC	3D	0.21	[80]
	$CsPbI_3$ NC	3D	1.1	[81]
	$CsPbBr_3/Cs_4PbBr_6$ NC	3D/0D	<10	[82]
	C_3PbBr_4 SC	2D	2.8	[83]
	C_6PbI_4 SC	2D	0.39	[83]
	BM_2PbBr_4 SC	2D	0.95	[84]
	$(EDBE)PbCl_4$ SC	2D	7.9	[18]
	PEA_2PbBr_4 SC	2D	14	[51]
	PEA_2PbBr_4 NC	2D	4.4	[85]
Lead-free halide perovskites	$CsEuI_3$ SC	3D	3.4×10^3	[86]
	$CsCaBrI_2:Eu^{2+}$ SC	3D	2.1×10^3	[87]
	$CsSrBrI_2:Eu^{2+}$ SC	3D	1.9×10^3	[87]
	$CsSrClB_2:Eu^{2+}$ SC	3D	3.5×10^3	[87]
	$(C_8H_{17}NH_3)_2SnBr_4$ SC	2D	3.34×10^3	[88]
	$Cs_4MnBi_2Cl_{12}$ SC	2D	144×10^3	[89]
Low-dimensional lead-free halide perovskites	$Cs_3Cu_2I_5:In^+$ SC	0D	fast components: 557 slow components: 3750	[90]
	Rb_2CuBr_3 SC	1D	41.4×10^3	[29]
	Rb_2CuCl_3 SC	1D	11.3×10^3	[91]
	Cs_4EuI_6 SC	0D	3.33×10^3	[92]
	Cs_4EuBr_6 SC	0D	3.72×10^3	[92]

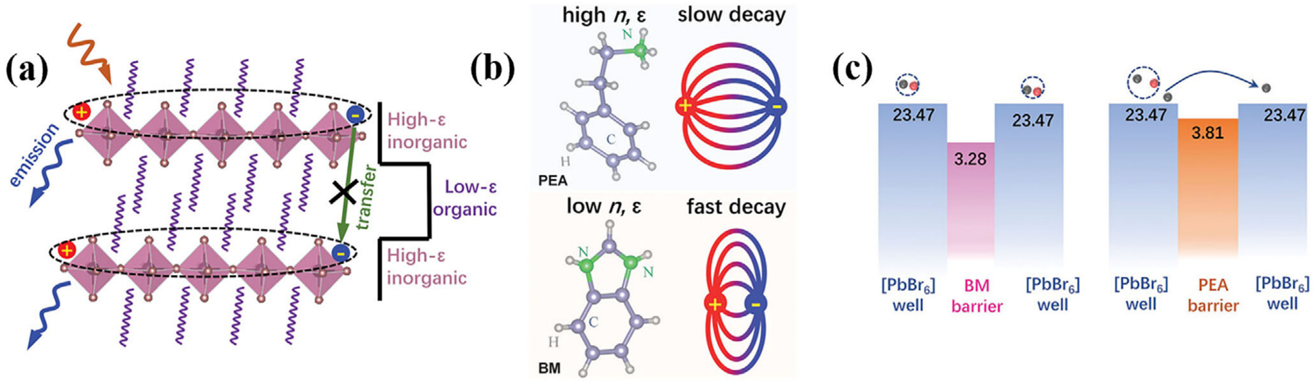

FIGURE 7 | (a) Crystal structure of 2D organic–inorganic hybrid perovskites with quantum well structure. (b) Design strategy for selecting organic amines with lower dielectric constant to enhance exciton confinement. (c) Dielectric distributions of $[PbBr_6]$ plane well and organic amines barrier for PEA_2PbBr_4 and BM_2PbBr_4. Reproduced with permission [84]. Copyright 2023, Wiley-VCH.

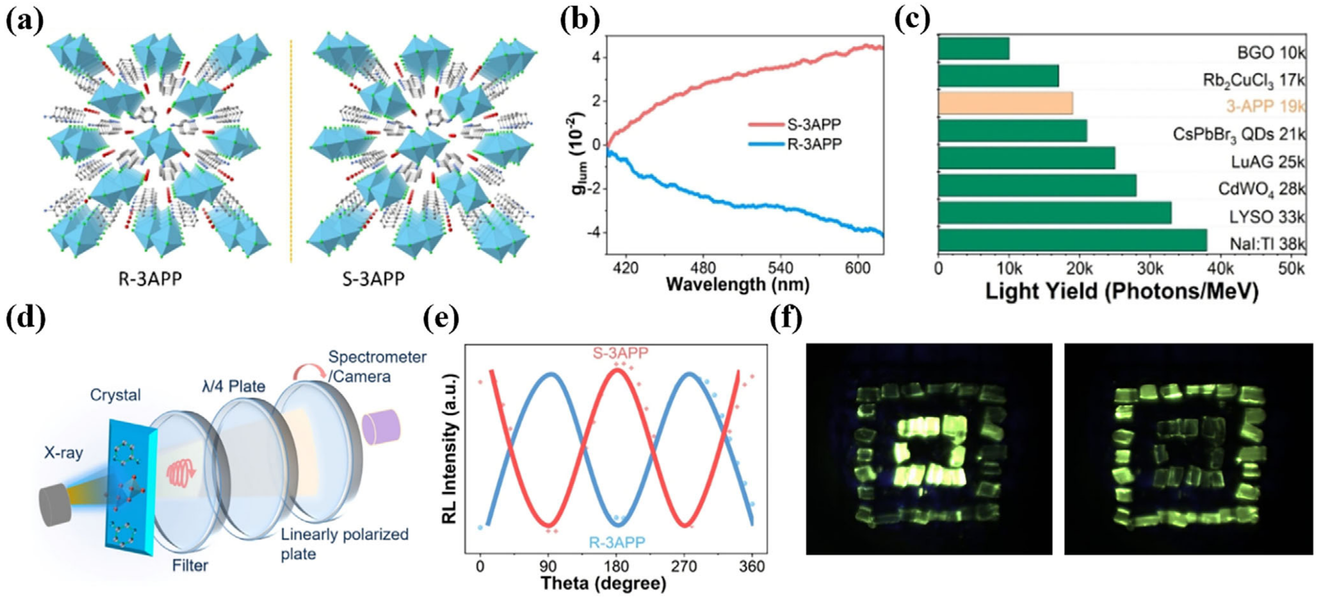

FIGURE 8 | (a) The crystal structures of R-3APP and S-3APP. (b) The luminescence dissymmetry factor (g_{lum}) values for R-3APP and S-3APP. (c) The light yield for 3-APP and several well-established scintillators. (d) Schematic diagram of the experimental setup for verifying polarized radioluminescence. (e) Polarization-dependent radioluminescence of chiral S-3APP and R-3APP. (f) The left-handed and right-handed luminescent crystals show bright and dark changes when rotating the linear polarizer. Reproduced with permission [99]. Copyright 2022, Wiley-VCH.

crystal configurations. This symmetry leads to the spatially uniform distribution of electric dipole transition vector directions during the luminescence process, and thus the stimulated radioluminescence displays isotropic characteristics. Wang et al. regulated the radioluminescence propagation by designing chiral perovskite-based scintillators (R-3AP)PbBr$_3$Cl·H$_2$O (R-3APP) and (S-3AP)PbBr$_3$Cl·H$_2$O (S-3APP) (Figure 8a), which had unique circularly polarized radioluminescence (CPRL) properties [99]. The strong spin-orbit coupling of heavy metals in perovskites endows them with high magnetic dipole moments. Consequently, the luminescence dissymmetric factors (g_{lum}) of S-3APP and R-3APP were as high as 4×10^{-2} and 3.6×10^{-2}, respectively (Figure 8b). Moreover, the light yield of 3APP was 19 000 photons/MeV, approximately twice that of BGO (Figure 8c). The research team leveraged a self-made polarized light collection system to explore the radioluminescence characteristics of chiral and non-chiral scintillators (Figure 8d). Interestingly, the RL intensities of S-3APP and R-3APP presented obvious polarization dependence, and the light propagation directions showed asymmetric oscillations (Figure 8e). To further verify the optical differences between S-3APP and R-3APP, the team fabricated a simple matrix. By alternately arranging left-handed and right-handed crystals, a series of chiral scintillators were assembled. Under x-ray irradiation, these crystals demonstrated clear contrast differences, indicating that the light propagation of each crystal was different (Figure 8f). This finding proposes a brand-new x-ray imaging scheme that can help improve imaging quality.

3.3.2 | Waveguide Effect

The waveguide effect is an optical phenomenon based on the principle of total internal reflection: when light is incident from a medium with a higher refractive index to one with a lower refractive index at an angle greater than the critical angle, it undergoes complete reflection within the dense medium and propagates along the interface without leakage [100]. By precisely designing the waveguide structure, the lateral diffusion of photons can be confined, ensuring the efficient transmission of optical signals within the waveguide.

Tang et al. initially embedded Cs$_3$Cu$_2$I$_5$ scintillator into anodic aluminum oxide (AAO) using a simple hot-pressing method to make a pixelated scintillator film (Cs$_3$Cu$_2$I$_5$-AAO) with a target thickness (Figure 9a) [101]. The AAO template has a porous structure and a low refractive index, which is conducive to constructing Cs$_3$Cu$_2$I$_5$ columnar crystals with a higher refractive index wrapped in an Al$_2$O$_3$ matrix. In this case, the Cs$_3$Cu$_2$I$_5$-AAO scintillator manifests a waveguide effect, promoting the propagation of scintillation light within Cs$_3$Cu$_2$I$_5$ by minimizing light scattering (Figure 9b,c). The spatial resolution of this film reached 10.4 lp/mm (MTF = 20%) (Figure 9d). To verify the light confinement effect of the designed pixelated Cs$_3$Cu$_2$I$_5$-AAO film, the light field distributions of HP-Cs$_3$Cu$_2$I$_5$ (Cs$_3$Cu$_2$I$_5$ thick film without AAO) and Cs$_3$Cu$_2$I$_5$-AAO at different thicknesses were analyzed by the finite-difference time-domain (FDTD) method (Figure 9e,f). As the film thickness increased, the emitted scintillation light of both HP-Cs$_3$Cu$_2$I$_5$ and Cs$_3$Cu$_2$I$_5$-AAO films became more dispersed. Notably, the integrated light intensity of Cs$_3$Cu$_2$I$_5$-AAO is greater than that of HP- Cs$_3$Cu$_2$I$_5$, demonstrating that Cs$_3$Cu$_2$I$_5$-AAO can effectively confine scintillation light.

3.3.3 | Increasing Transparency

Scintillator films formed by incorporating perovskite NCs into polymer matrices are prone to severe aggregation, primarily due to the notable disparity in hydrophilicity and hydrophobicity

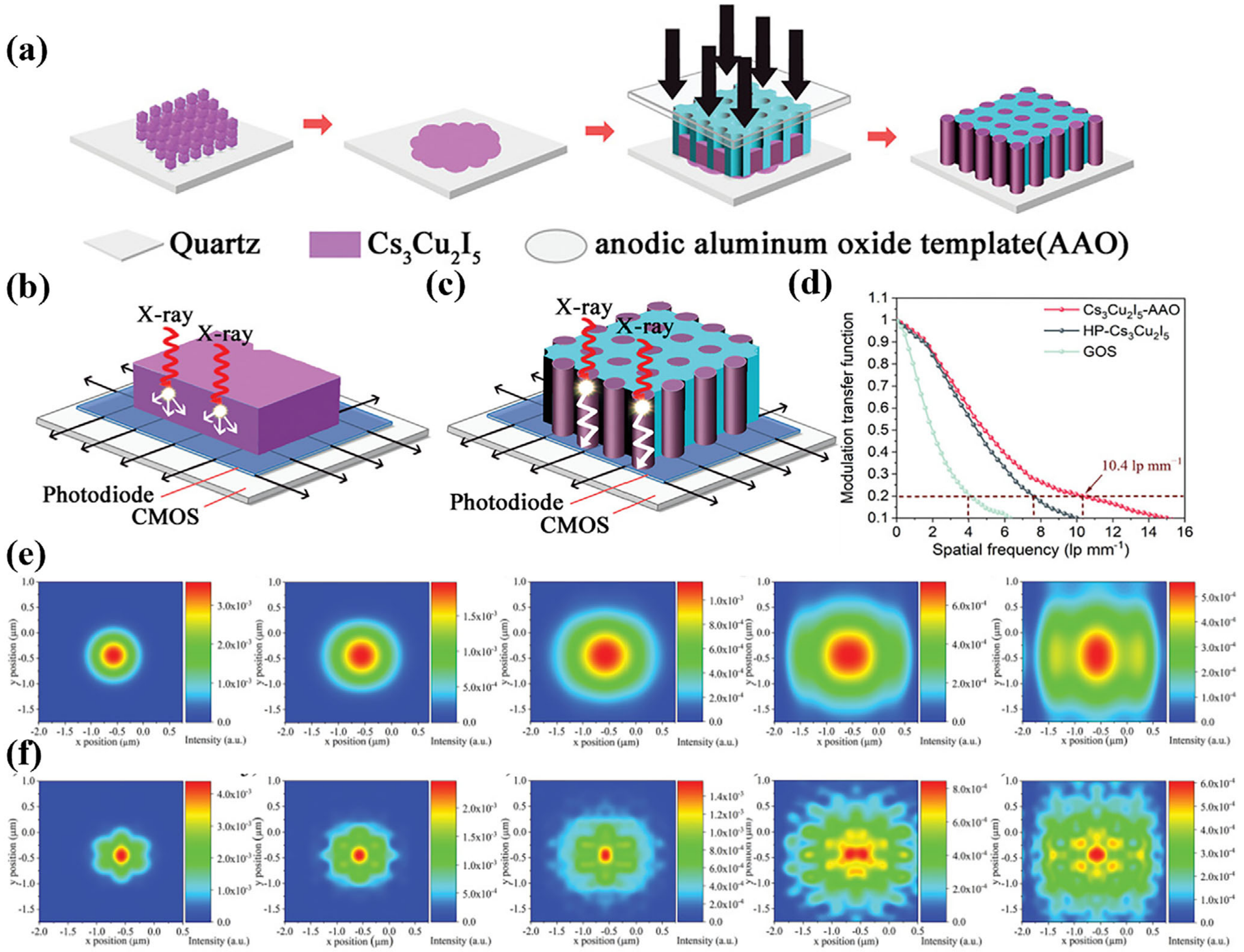

FIGURE 9 | (a) Schematic diagram of hot-pressing procedure for $Cs_3Cu_2I_5$-AAO film. (b,c) The scintillation light propagation paths of bulk $Cs_3Cu_2I_5$ film and pixelated $Cs_3Cu_2I_5$-AAO film. (d) The MTF values of $Cs_3Cu_2I_5$-AAO, HP-$Cs_3Cu_2I_5$, and GOS. The simulated distributions of internal scintillation light in (e) HP-$Cs_3Cu_2I_5$ and (f) $Cs_3Cu_2I_5$-AAO with different film thicknesses. Reproduced with permission [101]. Copyright 2021, Wiley-VCH.

between perovskite and the polymer host. This aggregation phenomenon induces light scattering and an inhomogeneous distribution of luminescence centers, ultimately causing a substantial reduction in the overall transparency of the composite film. To overcome this limitation, the current research focuses on precise ligand engineering and polymer matrix regulation to enhance compatibility, suppress aggregation, and achieve highly transparent and uniform composite scintillators (Table 4) [102–111]. Kuang et al. grew $CsPbBr_3$ NCs within a low-melting-point coordination polymer glass ($ZnBr_2(bIm+DMSO)_2$) through an in situ crystallization approach (Figure 10a) [102]. In the $CsPbBr_3@ZnBr_2(bIm+DMSO)_2$ glass, the high viscosity of the coordination polymer glass inhibits the migration-induced aggregation of perovskite NCs, realizing a transmittance exceeding 80% in the range of 500 to 800 nm (Figure 10b,c). Meanwhile, dimethyl sulfoxide (DMSO) as a solvent to dissolve CsBr and $PbBr_2$ benefits the uniform dispersion of $CsPbBr_3$ NCs. Utilizing the $CsPbBr_3@ZnBr_2(bIm+DMSO)_2$ glass as an x-ray imaging screen achieved a high imaging resolution of 25 lp/mm (Figure 10d,e), surpassing the resolution of most recently reported materials (Figure 10f). In addition, Xu et al. dissolved CsBr and $PbBr_2$ in DMF and then induced the nucleation and growth of $CsPbBr_3$ NCs in high-viscosity PMMA polymer via a thermal annealing process [104]. A high-performance polymer-ceramics scintillator with a spatial resolution of 12.5 lp/mm was achieved. The C-O-C in PMMA strongly coordinated with Pb^{2+}, inhibiting the migration and aggregation of ions. Under x-ray irradiation, even upon partial disruption of the $CsPbBr_3$ lattice, the majority of coordination bonds between the PMMA chains and Pb^{2+} were preserved, thereby confining Cs^+, Pb^{2+}, and Br^- ions to their original positions and preventing disordered diffusion. Subsequent low-temperature heat treatment supplied sufficient energy to facilitate recrystallization, using the residual nuclei as seeding sites. A surface modified-$CsPbBr_3$/polybutylmethacrylate (PBMA) nanocomposite was reported [103]. By introducing bis(2-(methacryloxy)ethyl) phosphate (BMEP), the ratio of the original ligand on the surface of $CsPbBr_3$ NCs was adjusted, which facilitated the uniform dispersion of $CsPbBr_3$ NCs within the polymer matrix. The BMEP-treated $CsPbBr_3$/PBMA nanocomposites demonstrated enhanced transmittance in the visible light spectrum compared to the untreated samples (Figure 10g,h). Furthermore, a series of well-resolved and clear x-ray images were

TABLE 4 | Scintillation properties of halide perovskite/polymer composites.

Materials	Synthesis method	Polymer	Light yield (ph/MeV)	Detection limit (nGy_{air}/s)	Spatial resolution (lp/mm)	Refs.
$CsPbBr_3$	In situ growth	$ZnBr_2(bIm+DMSO)_2$ glass	1202	514	25	[102]
$CsPbBr_3$	In situ growth	PMMA	15 800	120	12.5	[104]
$CsPbBr_3$	In situ growth	Dispersion: PBMA	——	4.6×10^3	——	[103]
$CsPbBr_3$	Ball milling	Dispersion: PMMA	——	——	8	[105]
$CsPbBr_3:Ce^{3+}$	Hot injection	Suction filtration: PVDF	33 000	——	580 (MTF = 0.2)	[106]
Cs_4PbBr_6	Solution mixing + Doctor blade/Drop casting/SLA	Dispersion: GDRB	10% of a commercial EJ232 scintillator	——	——	[107]
$Cs_3Cu_2I_5$	In situ growth	VmB1	55 521	326	14	[108]
$Cs_3Cu_2I_5:Tl$	In situ growth	PMMA	48 800	305	16.3	[109]
$(C_{24}H_{20}P)_2$-$MnBr_4$	In situ growth	Dispersion:TPU	——	608	14.5	[110]

*SLA = stereolithography; GDRB = GENESIS-DRB; VmB1 = vitamin B1.

obtained using BMEP-treated $CsPbBr_3$/PBMA nanocomposite scintillator at various dose rates ranging from 4.6 to 20.9 $\mu Gy_{air}/s$ (Figure 10i).

4 | Summary and Outlook

The vigorous development of x-ray detection technology is driving a revolutionary wave in the research of scintillator materials. HP materials have emerged as a promising candidate due to their excellent photoelectric properties. This review highlights the principal strategies for improving light yield and optimizing decay-response time, as well as approaches for controlling the propagation pathways of scintillation light. To better support practical applications, we analyze the research bottlenecks that must be overcome and point out the essential technologies needed to meet these obstacles.

- Lead-based perovskite scintillators have outstanding light yields and ultrafast decay times. However, the inherent lead toxicity not only causes severe environmental concerns but also poses serious threats to human health. Although numerous lead-free halide perovskites, such as $Cs_3Cu_2I_5$ and $Cs_2Ag_{0.6}Na_{0.4}In_{1\text{-}y}BiyCl_6$, have been developed by replacing lead with other high-Z elements and show extremely high light yields, their much longer decay times limit their applicability in rapid signal detection. An ideal HP scintillator should simultaneously possess high light yield, rapid response, excellent stability, and low toxicity. However, no single material currently satisfies all these requirements, as improving one property often compromises another. Therefore, the optimization of HP scintillators should be guided by specific application scenarios. For low-dose x-ray imaging, high light yield and low detection limit may be prioritized, whereas ultrafast decay times are more important for dynamic imaging and time-resolved applications. In addition, toxicity and environmental stability should also be taken into account for practical long-term use. To balance these competing factors, a dual-strategy approach is required. On one hand, existing lead-free perovskite materials should be further optimized to achieve a systematic coordination of performance parameters for specific applications. On the other hand, machine learning-assisted materials design can promote the development of new materials and the exploration of lead-free perovskite systems [112, 113]. By rapidly evaluating the thermodynamic stability, formability, and bandgap characteristics of candidate materials, machine learning can accelerate the discovery of promising lead-free perovskite scintillators while reducing reliance on conventional trial-and-error experimental approaches.
- The radiation tolerance of HP scintillators cannot be ignored, especially under high-dose x-ray irradiation. Long-term irradiation may trigger the breakage of chemical bonds, degradation of organic components, and the accumulation of lattice defects, resulting in reduced light yield, decreased energy resolution, and deteriorated long-term stability. Implementing a multi-scale optimization strategy offers an effective way to enhance the radiation tolerance of HP scintillators. At the material level, the introduction of specific dopants or adjustments to the chemical composition can stabilize the lattice structure and suppress defect formation. Interface engineering, such as constructing core-shell structures or embedding high-Z nanoparticles, can further scatter secondary electrons to improve the radiation tolerance. At the device level, the design of heterojunctions (e.g., multilayer stacking structures) leverages the synergistic effects of different materials to mitigate radiation damage.
- Advanced medical imaging techniques impose strict requirements on the response-decay time of scintillator materials. A

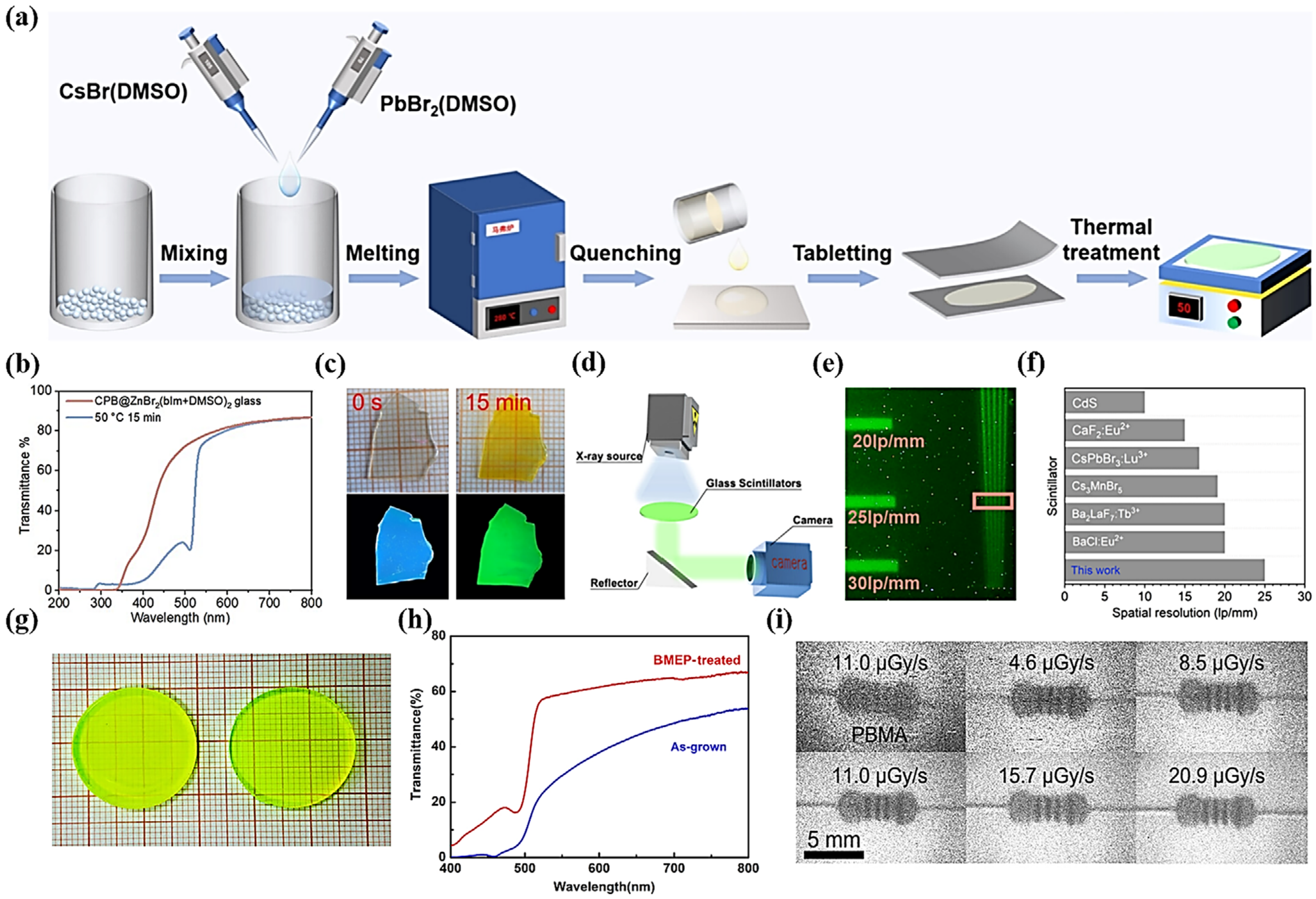

FIGURE 10 | (a) Schematic diagram of the preparation process for $CsPbBr_3@ZnBr_2(bIm+DMSO)_2$ glass. (b) Ultraviolet-visible transmittance spectra of $CsPbBr_3@ZnBr_2(bIm+DMSO)_2$ glass before and after heat treatment at 50°C for 15 min. (c) Photographs of $CsPbBr_3@ZnBr_2(bIm+DMSO)_2$ glasses after being placed on a hot plate at 50°C for 0s and 15 min under daylight and UV illumination. (d) Schematic illustration of the designed x-ray scintillator imaging system. (e) X-ray imaging of the lead line pair card. (f) Comparison with the spatial resolution of representative scintillators. Reproduced with permission [102]. Copyright 2025, American Chemical Society. (g) Photographs of $CsPbBr_3$/PBMA nanocomposites without (left) and with (right) BMEP treatment. (h) Transmission spectra of $CsPbBr_3$/PBMA nanocomposites without/with BMEP treatment. (i) X-ray images of the resistance collected under a series of x-ray dose rates. Reproduced with permission [103]. Copyright 2021, American Chemical Society.

sub-nanosecond (<1 ns) response time is an important parameter for improving time resolution and reducing motion artifacts. Though HP scintillators have shown advantages with nanosecond-level decay lifetimes, comprehensive studies on further shortening their luminescent decay remain scarce. Recent studies have manifested that dielectric engineering, an emerging technical approach, offers an innovative solution to this challenge. By introducing high dielectric constant dielectric layers into scintillator materials, researchers can effectively tune the dielectric environment to decrease exciton binding energy. This approach accelerates charge separation and recombination processes, ultimately enabling ultrafast scintillation with sub-nanosecond decay times.

HP scintillators are currently undergoing a crucial transition from laboratory-based proof-of-concept studies to application-oriented prototypes. Despite their superior performance in certain metrics compared with traditional materials, lead toxicity and structural instability remain key challenges limiting their commercialization. Further breakthroughs in device lifetime, encapsulation, cost-effectiveness, large-area fabrication, and compatibility with commercial imaging systems are still required before HP scintillators can replace established commercial scintillators.

Acknowledgements

This research was supported by the National Natural Science Foundation of China (52572155, 52272141), and the Natural Science Foundation of Fujian Province (2024J02014, 2024J01949).

Conflicts of Interest

The authors declare no conflicts of interest.

Data Availability Statement

Research data are not shared.

References

1. S.-A. Zhou and A. Brahme, “Development of Phase-Contrast X-Ray Imaging Techniques and Potential Medical Applications,” *Physica Medica* 24 (2008): 129–148, https://doi.org/10.1016/j.ejmp.2008.05.006.

2. Y. Wu, J. Feng, Z. Yang, Y. Liu, and S. Liu, “Halide Perovskite: A Promising Candidate for Next-Generation X-Ray Detectors,” *Advanced Science* 10 (2023): 2205536, https://doi.org/10.1002/advs.202205536.

3. J. Fan, W. Li, Q. Zhou, et al., “Metal Halide Perovskites for Direct X-Ray Detection in Medical Imaging: To Higher Performance,” *Advanced Functional Materials* 35 (2025): 2401017, https://doi.org/10.1002/adfm.202401017.

4. Y. Su, W. Ma, and Y. Yang, “Perovskite Semiconductors for Direct X-Ray Detection and Imaging,” *Journal of Semiconductors* 41 (2020): 051204, https://doi.org/10.1088/1674-4926/41/5/051204.

5. C. Szeles, “CdZnTe and CdTe Materials for X-Ray and Gamma Ray Radiation Detector Applications,” *physica status solidi (b)* 241 (2004): 783–790, https://doi.org/10.1002/pssb.200304296.

6. A. Owens and A. Peacock, “Compound Semiconductor Radiation Detectors,” *Nuclear Instruments and Methods in Physics Research Section A: Accelerators, Spectrometers, Detectors and Associated Equipment* 531 (2004): 18–37, https://doi.org/10.1016/j.nima.2004.05.071.

7. M. Schieber, A. Zuck, H. Gilboa, and G. Zentai, “Reviewing Polycrystalline Mercuric Iodide X-Ray Detectors,” *IEEE Transactions on Nuclear Science* 53 (2006): 2385–2391, https://doi.org/10.1109/TNS.2006.877043.

8. Y. Chen, G. Zhang, F. Chen, et al., “Correction: Halogen-Bonded Charge-Transfer Co-Crystal Scintillators for High-Resolution X-Ray Imaging,” *Chemical Science* 15 (2024): 8249, https://doi.org/10.1039/D4SC90091J.

9. S.-Y. Yang, L. Zhang, F.-C. Kong, et al., “Scintillators with Aggregation-Induced Emission,” *Chemistry* 11 (2025): 102534, https://doi.org/10.1016/j.chempr.2025.102534.

10. Y. Zhou, J. Chen, O. M. Bakr, and O. F. Mohammed, “Metal Halide Perovskites for X-ray Imaging Scintillators and Detectors,” *ACS Energy Letters* 6 (2021): 739–768, https://doi.org/10.1021/acsenergylett.0c02430.

11. G. Blasse, “Scintillator Materials,” *Chemistry of Materials* 6 (1994): 1465–1475, https://doi.org/10.1021/cm00045a002.

12. C. Michail, I. Valais, I. Seferis, et al., “Measurement of the Luminescence Properties of Gd_2O_2S:Pr,Ce,F Powder Scintillators under X-ray Radiation,” *Radiation Measurements* 70 (2014): 59–64, https://doi.org/10.1016/j.radmeas.2014.09.008.

13. S. Blahuta, B. Viana, A. Bessiere, F. Mattmann, and B. LaCourse, “Luminescence Quenching Processes in $Gd_2O_2S:Pr^{3+},Ce^{3+}$ Scintillating Ceramics,” *Optical Materials* 33 (2011): 1514–1518, https://doi.org/10.1016/j.optmat.2011.02.040.

14. T. Wang, G. Zeng, Y. Yang, et al., “Advances in Metal Halide Perovskite Scintillators for X-Ray Detection,” *Nano-Micro Letters* 17 (2025): 275, https://doi.org/10.1007/s40820-025-01772-7.

15. H. Hall, “The Theory of Photoelectric Absorption for X-Rays and γ -Rays,” *Reviews of Modern Physics* 8 (1936): 358–397, https://doi.org/10.1103/RevModPhys.8.358.

16. J. Liu, B. Shabbir, C. Wang, et al., “Flexible, Printable Soft-X-Ray Detectors Based on All-Inorganic Perovskite Quantum Dots,” *Advanced Materials* 31 (2019): 1901644, https://doi.org/10.1002/adma.201901644.

17. W. Pan, B. Yang, G. Niu, et al., “Hot-Pressed $CsPbBr_3$ Quasi-Monocrystalline Film for Sensitive Direct X-ray Detection,” *Advanced Materials* 31 (2019): 1904405, https://doi.org/10.1002/adma.201904405.

18. M. D. Birowosuto, D. Cortecchia, W. Drozdowski, et al., “X-ray Scintillation in Lead Halide Perovskite Crystals,” *Scientific Reports* 6 (2016): 37254.

19. J. Lin, Y. Lu, X. Li, et al., “Perovskite Quantum Dots Glasses Based Backlit Displays,” *ACS Energy Letters* 6 (2021): 519–528, https://doi.org/10.1021/acsenergylett.0c02561.

20. S. Chen, J. Lin, J. Huang, et al., “CsPbBr 3 @Glass Nanocomposite With Green-Emitting External Quantum Efficiency of 75% for Backlit Display,” *Advanced Functional Materials* 34 (2024): 2309293, https://doi.org/10.1002/adfm.202309293.

21. S. Chen, J. Lin, S. Zheng, Y. Zheng, and D. Chen, “Efficient and Stable Perovskite White Light-Emitting Diodes for Backlit Display,” *Advanced Functional Materials* 33 (2023): 2213442, https://doi.org/10.1002/adfm.202213442.

22. K. Wang, Z. Jin, L. Liang, et al., “All-Inorganic Cesium Lead Iodide Perovskite Solar Cells with Stabilized Efficiency beyond 15%,” *Nature Communications* 9 (2018): 4544, https://doi.org/10.1038/s41467-018-06915-6.

23. Q. Chen, J. Wu, X. Ou, et al., “All-Inorganic Perovskite Nanocrystal Scintillators,” *Nature* 561 (2018): 88–93, https://doi.org/10.1038/s41586-018-0451-1.

24. J. H. Heo, D. H. Shin, J. K. Park, D. H. Kim, S. J. Lee, and S. H. Im, “High-Performance Next-Generation Perovskite Nanocrystal Scintillator for Nondestructive X-Ray Imaging,” *Advanced Materials* 30 (2018): 1801743, https://doi.org/10.1002/adma.201801743.

25. W. Zhu, W. Ma, Y. Su, et al., “Low-Dose Real-Time X-Ray Imaging with Nontoxic Double Perovskite Scintillators,” *Light: Science & Applications* 9 (2020): 112, https://doi.org/10.1038/s41377-020-00353-0.

26. Y. Jiao, R. Li, H. Wang, et al., “Bright and Fast-Response Hybrid X-Ray Scintillators by Molecular and Dielectric Confinement,” *Angewandte Chemie International Edition* 64 (2025): e202504576.

27. W. Shao, X. Wang, Z. Zhang, et al., “Highly Efficient and Flexible Scintillation Screen based on Manganese (II) Activated 2D Perovskite for Planar and Nonplanar High-Resolution X-Ray Imaging,” *Advanced Optical Materials* 10 (2022): 2102282.

28. T. He, Y. Zhou, X. Wang, et al., “High-Performance Copper-Doped Perovskite-Related Silver Halide X-ray Imaging Scintillator,” *ACS Energy Letters* 7 (2022): 2753–2760, https://doi.org/10.1021/acsenergylett.2c01484.

29. B. Yang, L. Yin, G. Niu, et al., “Lead-Free Halide Rb_2CuBr_3 as Sensitive X-Ray Scintillator,” *Advanced Materials* 31 (2019): 1904711, https://doi.org/10.1002/adma.201904711.

30. L. Lian, M. Zheng, W. Zhang, et al., “Efficient and Reabsorption-Free Radioluminescence in $Cs_3Cu_2I_5$ Nanocrystals With Self-Trapped Excitons,” *Advanced Science* 7 (2020): 2000195, https://doi.org/10.1002/advs.202000195.

31. F. Zhang, Y. Zhou, Z. Chen, et al., “Thermally Activated Delayed Fluorescence Zirconium-Based Perovskites for Large-Area and Ultraflexible X-ray Scintillator Screens,” *Advanced Materials* 34 (2022): 2204801, https://doi.org/10.1002/adma.202204801.

32. F. Zhang, Y. Zhou, Z. Chen, et al., “Large-Area X-Ray Scintillator Screen Based on Cesium Hafnium Chloride Microcrystals Films With High Sensitivity and Stability,” *Laser & Photonics Reviews* 17 (2023): 2200848, https://doi.org/10.1002/lpor.202200848.

33. T. He, Y. Zhou, P. Yuan, et al., “Copper Iodide Inks for High-Resolution X-ray Imaging Screens,” *ACS Energy Letters* 8 (2023): 1362–1370, https://doi.org/10.1021/acsenergylett.3c00097.

34. J. H. Han, T. Samanta, Y. M. Park, et al., “Highly Stable Zero-Dimensional Lead-Free Metal Halides for X-Ray Imaging,” *ACS Energy Letters* 8 (2023): 545–552, https://doi.org/10.1021/acsenergylett.2c02469.

35. M. Moszynski, M. Kapusta, M. Mayhugh, D. Wolski, and S. O. Flyckt, “Absolute Light Output of Scintillators,” *IEEE Transactions on Nuclear Science* 44 (1997): 1052–1061, https://doi.org/10.1109/23.603803.

36. G. F. Knoll, Radiation Detection and Measurement (Wiley, 2010).

37. X. Zhu, R. Zhou, Z. Wang, et al., “Lanthanide-Metal-Doped Light-Harvesting Quantum Dots for Exceptional X-ray Imaging Scintillators,” *ACS Energy Letters* 9 (2024): 5137–5144, https://doi.org/10.1021/acsenergylett.4c02155.

38. X. Du, S. Zhao, L. Wang, et al., “Efficient and Ultrafast Organic Scintillators by Hot Exciton Manipulation,” *Nature Photonics* 18 (2024): 162–169, https://doi.org/10.1038/s41566-023-01358-y.

39. E. Montbaron, F. Sguerra, G. H. V. Bertrand, et al., “N -(2-Ethylhexyl)carbazole: A New Fluorophore Highly Suitable as a Monomolecular Liquid Scintillator,” *Chemistry—A European Journal* 22 (2016): 12074–12080, https://doi.org/10.1002/chem.201601749.

40. X. Wen, Y. Wang, R. Kucerkova, et al., “Energy Transfer Engineering Enabled Efficient and Broad-Band Near-Infrared Emission,” *ACS Energy Letters* 10 (2025): 3681–3688, https://doi.org/10.1021/acsenergylett.5c01712.

41. K. Shibuya, M. Koshimizu, Y. Takeoka, and K. Asai, “Scintillation Properties of (C6H13NH3)2PbI4: Exciton Luminescence of an Organic/Inorganic Multiple Quantum Well Structure Compound Induced by 2.0 MeV Protons,” *Nuclear Instruments and Methods in Physics Research Section B: Beam Interactions with Materials and Atoms* 194 (2002): 207–212, https://doi.org/10.1016/S0168-583X(02)00671-7.

42. F. Zhou, Z. Li, W. Lan, Q. Wang, L. Ding, and Z. Jin, “Halide Perovskite, a Potential Scintillator for X-Ray Detection,” *Small Methods* 4 (2020): 2000506, https://doi.org/10.1002/smtd.202000506.

43. H. Jin, S. Yang, M. A. Iqbal, and Y. Zeng, “Metal Halide Perovskite Nanocrystals for X-Ray Scintillators,” *Nano Futures* 6 (2022): 042001, https://doi.org/10.1088/2399-1984/ac9568.

44. O. Balitskii, M. Sytnyk, and W. Heiss, “Recent Developments in Halide Perovskite Nanocrystals for Indirect X-ray Detection,” *Advanced Materials Technologies* 9 (2024): 2400150, https://doi.org/10.1002/admt.202400150.

45. M. Nikl, “Scintillation Detectors for X-Rays,” *Measurement Science and Technology* 17 (2006): R37–R54, https://doi.org/10.1088/0957-0233/17/4/R01.

46. H. Wu, Y. Ge, and J. Tang, “Metal Halide Perovskites for X-Ray Detection and Imaging,” *Matter* 4 (2021): 144–163, https://doi.org/10.1016/j.matt.2020.11.015.

47. F. Maddalena, L. Tjahjana, A. Xie, et al., “Inorganic, Organic, and Perovskite Halides With Nanotechnology for High–Light Yield X- and γ-ray Scintillators,” *Crystals* 9 (2019): 88, https://doi.org/10.3390/cryst9020088.

48. H. Wei and J. Huang, “Halide Lead Perovskites for Ionizing Radiation Detection,” *Nature Communications* 10 (2019): 1066, https://doi.org/10.1038/s41467-019-08981-w.

49. A. Xie, T. H. Nguyen, C. Hettiarachchi, et al., “Thermal Quenching and Dose Studies of X-ray Luminescence in Single Crystals of Halide Perovskites,” *The Journal of Physical Chemistry C* 122 (2018): 16265–16273, https://doi.org/10.1021/acs.jpcc.8b03622.

50. L. Mao, C. C. Stoumpos, and M. G. Kanatzidis, “Two-Dimensional Hybrid Halide Perovskites: Principles and Promises,” *Journal of the American Chemical Society* 141 (2019): 1171–1190, https://doi.org/10.1021/jacs.8b10851.

51. B. Jia, D. Chu, N. Li, et al., “Airflow-Controlled Crystallization for a Multi-Inch 2D Halide Perovskite Single-Crystal Scintillator for Fast High-Resolution X-ray Imaging,” *ACS Energy Letters* 8 (2022): 590–599, https://doi.org/10.1021/acsenergylett.2c02196.

52. Y. Zhang, R. Sun, X. Qi, et al., “Metal Halide Perovskite Nanosheet for X-ray High-Resolution Scintillation Imaging Screens,” *ACS Nano* 13 (2019): 2520–2525, https://doi.org/10.1021/acsnano.8b09484.

53. W. Chen, Y. Liu, Z. Yuan, et al., “X-Ray Radioluminescence Effect of All-Inorganic Halide Perovskite CsPbBr$_3$ Quantum Dots,” *Journal of Radioanalytical and Nuclear Chemistry* 314 (2017): 2327–2337, https://doi.org/10.1007/s10967-017-5562-x.

54. H. Zhang, Z. Yang, M. Zhou, et al., “Reproducible X-ray Imaging With a Perovskite Nanocrystal Scintillator Embedded in a Transparent Amorphous Network Structure,” *Advanced Materials* 33 (2021): 2102529, https://doi.org/10.1002/adma.202102529.

55. L. Zi, J. Song, N. Wang, et al., “X-Ray Quantum Cutting Scintillator Based on CsPbCl$_x$Br$_{3-x}$:Yb^{3+} Single Crystals,” *Laser & Photonics Reviews* 17 (2023): 2200852, https://doi.org/10.1002/lpor.202200852.

56. K. Li, W. Zhang, L. Niu, Y. Ye, J. Ren, and C. Liu, “Lead-Free Cesium Manganese Halide Nanocrystals Embedded Glasses for X-Ray Imaging,” *Advanced Science* 10 (2023): 2204843, https://doi.org/10.1002/advs.202204843.

57. X. Ge, Q. Zhang, T. Fei, Y. Wu, L. Luo, and P. Du, “Designing Polychromatic Luminescence in Mn^{2+} -Doped Cs$_2$ NaLuCl$_6$ Double Perovskite Crystals via Energy Transfer Engineering for Optical Thermometry and X-ray Imaging,” *Inorganic Chemistry* 64 (2025): 3038–3047, https://doi.org/10.1021/acs.inorgchem.4c05370.

58. H. Xu, W. Liang, Z. Zhang, et al., “2D Perovskite Mn 2+ -Doped Cs$_2$CdBr$_2$Cl$_2$ Scintillator for Low-Dose High-Resolution X-Ray Imaging,” *Advanced Materials* 35 (2023): 2300136, https://doi.org/10.1002/adma.202300136.

59. C. Wang, Z. Yan, Y. Wang, et al., “All-Inorganic Ruddlesden–Popper Perovskite Cs$_2$CdCl$_4$:Mn for Low-Dose and Flexible X-ray Imaging,” *ACS Materials Letters* 6 (2024): 1429–1438, https://doi.org/10.1021/acsmaterialslett.3c01665.

60. J. Zheng, Z. Zhou, T. Feng, et al., “Hydrophobic Long-Chain Two-Dimensional Perovskite Scintillators for Underwater X-Ray Imaging,” *Rare Metals* 43 (2024): 175–185, https://doi.org/10.1007/s12598-023-02421-x.

61. J. Jin, K. Han, Y. Hu, and Z. Xia, “Zn^{2+} Doping in Organic Manganese(II) Bromide Hybrid Scintillators Toward Enhanced Light Yield for X-Ray Imaging,” *Advanced Optical Materials* 11 (2023): 2300330, https://doi.org/10.1002/adom.202300330.

62. B. Wang, X. Ou, X. He, Z. Deng, Y. Zhou, and P. Li, “High-Resolution X-Ray Imaging of Mn Enhanced Lead-Free Halide Scintillators in Pixelated Array Structures,” *Advanced Optical Materials* 11 (2023): 2300388, https://doi.org/10.1002/adom.202300388.

63. B. Su, K. Han, and Z. Xia, “Mn^{2+} -doped Cs$_2$ZnBr$_4$ Scintillator for X-Ray Imaging,” *Journal of Materials Chemistry C* 11 (2023): 8052–8061, https://doi.org/10.1039/D2TC04249E.

64. W. Ma, T. Jiang, Z. Yang, et al., “Highly Resolved and Robust Dynamic X-Ray Imaging Using Perovskite Glass-Ceramic Scintillator With Reduced Light Scattering,” *Advanced Science* 8 (2021): 2003728, https://doi.org/10.1002/advs.202003728.

65. Z. Wang, X. Xu, S. Wang, et al., “Cerium Doping Double Perovskite Scintillator for Sensitive X-ray Detection and Imaging,” *Chemistry–A European Journal* 27 (2021): 9071–9076.

66. L. Stand, M. Zhuravleva, B. Chakoumakos, et al., “Crystal Growth and Scintillation Properties of Eu^{2+} doped Cs$_4$CaI$_6$ and Cs$_4$SrI$_6$,” *Journal of Crystal Growth* 486 (2018): 162–168, https://doi.org/10.1016/j.jcrysgro.2018.01.017.

67. M. D. Smith and H. I. Karunadasa, “White-Light Emission From Layered Halide Perovskites,” *Accounts of Chemical Research* 51 (2018): 619–627, https://doi.org/10.1021/acs.accounts.7b00433.

68. V. Naresh, P.-R. Cha, and N. Lee, “Cs$_2$NaGdCl$_6$:Tb^{3+} —A Highly Luminescent Rare-Earth Double Perovskite Scintillator for Low-Dose X-ray Detection and Imaging,” *ACS Applied Materials & Interfaces* 16 (2024): 19068–19080, https://doi.org/10.1021/acsami.3c17301.

69. M. Gandini, I. Villa, M. Beretta, et al., “Efficient, Fast and Reabsorption-Free Perovskite Nanocrystal-Based Sensitized Plastic Scintillators,” *Nature Nanotechnology* 15 (2020): 462–468, https://doi.org/10.1038/s41565-020-0683-8.

70. Z. Wang, S. Li, G. Ren, et al., “Flexible and Reabsorption-Free Perovskite Scintillators for Low-Dose X-ray Detection and High-Resolution Imaging,” *ACS Photonics* 11 (2024): 3003–3011, https://doi.org/10.1021/acsphotonics.4c00117.

71. R. Li, W. Zhu, H. Wang, et al., "Ultrastable and Flexible Glass–Ceramic Scintillation Films with Reduced Light Scattering for Efficient X–Ray Imaging," *npj Flexible Electronics* 8 (2024): 31, https://doi.org/10.1038/s41528-024-00319-x.

72. Y. Tong, Q. Wang, H. Yang, et al., "Enhanced Multimodal Luminescence and Ultrahigh Stability Eu $^{3+}$ -doped $CsPbBr_3$ Glasses for X-Ray Detection and Imaging," *Photonics Research* 9 (2021): 2369, https://doi.org/10.1364/PRJ.439744.

73. W. Li, X. Wang, Y. Huang, and D. Kuang, "Ultrasound-Assisted Crystallization Enables Large-Area Perovskite Quasi-Monocrystalline Film for High-Sensitive X-ray Detection and Imaging," *Advanced Materials* 35 (2023): 2210878, https://doi.org/10.1002/adma.202210878.

74. B. Yang, X. Ouyang, X. Zhao, et al., "Inch-Sized 2D Perovskite Single-Crystal Scintillators for High-Resolution Neutron and X-Ray Imaging," *InfoMat* 7 (2025): 12648, https://doi.org/10.1002/inf2.12648.

75. C. Dujardin, E. Auffray, E. Bourret-Courchesne, et al., "Needs, Trends, and Advances in Inorganic Scintillators," *IEEE Transactions on Nuclear Science* 65 (2018): 1977–1997, https://doi.org/10.1109/TNS.2018.2840160.

76. Q. Xu, W. Shao, J. Liu, et al., "Bulk Organic–Inorganic Methylammonium Lead Halide Perovskite Single Crystals for Indirect Gamma Ray Detection," *ACS Applied Materials & Interfaces* 11 (2019): 47485–47490, https://doi.org/10.1021/acsami.9b10367.

77. K. Watanabe, M. Koshimizu, T. Yanagida, and Y. Fujimoto, "Clarification and Mitigation of Marked J c Decrease at Low Magnetic Fields of $BaHfO_3$ -doped $SmBaCuO_3$ Thin Films Deposited on Seed Layer," *Japanese Journal of Applied Physics* 55 (2016): 073101, https://doi.org/10.7567/JJAP.55.073101.

78. Y. Li, W. Shao, X. Ouyang, et al., "Scintillation Properties of Perovskite Single Crystals," *The Journal of Physical Chemistry C* 123 (2019): 17449–17453, https://doi.org/10.1021/acs.jpcc.9b05269.

79. V. B. Mykhaylyk, H. Kraus, V. Kapustianyk, et al., "Bright and Fast Scintillations of an Inorganic Halide Perovskite $CsPbBr_3$ Crystal at Cryogenic Temperatures," *Scientific Reports* 10 (2020): 8601.

80. A. Erroi, F. Carulli, F. Cova, et al., "Ultrafast Nanocomposite Scintillators Based on Cd-Enhanced $CsPbCl_3$ Nanocrystals in Polymer Matrix," *ACS Energy Letters* 9 (2024): 2333–2342, https://doi.org/10.1021/acsenergylett.4c00778.

81. F. Maddalena, A. Z. Xie, X. Y. Chin, et al., "Deterministic Light Yield, Fast Scintillation, and Microcolumn Structures in Lead Halide Perovskite Nanocrystals," *The Journal of Physical Chemistry C* 125 (2021): 14082–14088, https://doi.org/10.1021/acs.jpcc.1c03392.

82. Q. Xu, J. Wang, W. Shao, et al., "A Solution-Processed Zero-Dimensional All-Inorganic Perovskite Scintillator for High Resolution Gamma-Ray Spectroscopy Detection," *Nanoscale* 12 (2020): 9727–9732, https://doi.org/10.1039/D0NR00772B.

83. K. Shibuya, M. Koshimizu, H. Murakami, Y. Muroya, Y. Katsumura, and K. Asai, "Development of Ultra-Fast Semiconducting Scintillators Using Quantum Confinement Effect," *Japanese Journal of Applied Physics* 43 (2004): L1333–L1336, https://doi.org/10.1143/JJAP.43.L1333.

84. M. Xia, Z. Xie, H. Wang, et al., "Sub-Nanosecond 2D Perovskite Scintillators by Dielectric Engineering," *Advanced Materials* 35 (2023): 2211769, https://doi.org/10.1002/adma.202211769.

85. N. Kawano, K. Shinozaki, D. Nakauchi, H. Kimura, and T. Yanagida, "Scintillation Properties of Organic–Inorganic Layered Perovskite Nanocrystals in Glass," *Journal of Applied Physics* 127 (2020): 213103, https://doi.org/10.1063/5.0007084.

86. K. Yang, M. Zhuravleva, and C. L. Melcher, "Crystal Growth and Characterization of $CsSr_{1-x}Eu_xI_3$ High Light Yield Scintillators," *physica status solidi (RRL)—Rapid Research Letters* 5 (2011): 43–45, https://doi.org/10.1002/pssr.201004434.

87. L. Stand, M. Zhuravleva, B. Chakoumakos, et al., "Characterization of Mixed Halide Scintillators: $CsSrBrI_2$:Eu, $CsCaBrI_2$:Eu and $CsSrClBr_2$:Eu," *Journal of Luminescence* 207 (2019): 70–77, https://doi.org/10.1016/j.jlumin.2018.10.108.

88. J. T. Cao, Z. Guo, S. Zhu, et al., "Preparation of Lead-free Two-Dimensional-Layered $(C_8H_{17}NH_3)_2SnBr_4$ Perovskite Scintillators and Their Application in X-ray Imaging," *ACS Applied Materials & Interfaces* 12 (2020): 19797–19804, https://doi.org/10.1021/acsami.0c02116.

89. J. Wei, J. Liao, X. Wang, L. Zhou, Y. Jiang, and D. Kuang, "All-Inorganic Lead-Free Heterometallic $Cs_4MnBi_2Cl_{12}$ Perovskite Single Crystal with Highly Efficient Orange Emission," *Matter* 3 (2020): 892–903.

90. Q. Wang, Q. Zhou, M. Nikl, et al., "Highly Resolved X-Ray Imaging Enabled by In(I) Doped Perovskite-Like $Cs_3Cu_2I_5$ Single Crystal Scintillator," *Advanced Optical Materials* 10 (2022): 2200304, https://doi.org/10.1002/adom.202200304.

91. X. Zhao, G. Niu, J. Zhu, et al., "All-Inorganic Copper Halide as a Stable and Self-Absorption-Free X-ray Scintillator," *The Journal of Physical Chemistry Letters* 11 (2020): 1873–1880, https://doi.org/10.1021/acs.jpclett.0c00161.

92. Y. Wu, D. Han, B. C. Chakoumakos, et al., "Zero-Dimensional $Cs_4EuX_6(X = Br, I)$ All-Inorganic Perovskite Single Crystals for Gamma-Ray Spectroscopy," *Journal of Materials Chemistry C* 6 (2018): 6647–6655, https://doi.org/10.1039/C8TC01458B.

93. S. D. Stranks, G. E. Eperon, G. Grancini, et al., "Electron-Hole Diffusion Lengths Exceeding 1 Micrometer in an Organometal Trihalide Perovskite Absorber," *Science* 342 (2013): 341–344, https://doi.org/10.1126/science.1243982.

94. L. Dou, A. B. Wong, Y. Yu, et al., "Atomically Thin Two-Dimensional organic-inorganic Hybrid Perovskites," *Science* 349 (2015): 1518–1521, https://doi.org/10.1126/science.aac7660.

95. H. Peng, Y. Tian, X. Wang, et al., "Large-Scale Facile-Synthesis and Bistable Emissions of One-Dimensional Organic–Inorganic $C_4H_{14}N_2PbBr_4$ Metal Halide Crystals with Bipolaronic States," *New Journal of Chemistry* 45 (2021): 17247–17257, https://doi.org/10.1039/D1NJ03064G.

96. A. Gola, A. Ferri, A. Tarolli, N. Zorzi, and C. Piemonte, "SiPM Optical Crosstalk Amplification Due to Scintillator Crystal: Effects on Timing Performance," *Physics in Medicine and Biology* 59 (2014): 3615–3635, https://doi.org/10.1088/0031-9155/59/13/3615.

97. H. Sabet, G. Prekas, M. Breen, et al., "High-Performance and Cost-Effective Detector Using Microcolumnar CsI:Tl and SiPM," *IEEE Transactions on Nuclear Science* 59 (2012): 1841–1849, https://doi.org/10.1109/TNS.2012.2202248.

98. P. Buechele, M. Richter, S. F. Tedde, et al., "X-Ray Imaging with Scintillator-Sensitized Hybrid Organic Photodetectors," *Nature Photonics* 9 (2015): 843–848, https://doi.org/10.1038/nphoton.2015.216.

99. M. Li, Y. Wang, L. Yang, Z. Chai, Y. Wang, and S. Wang, "Circularly Polarized Radioluminescence from Chiral Perovskite Scintillators for Improved X-Ray Imaging," *Angewandte Chemie International Edition* 61 (2022): 202208440, https://doi.org/10.1002/anie.202208440.

100. R. Halir, P. J. Bock, P. Cheben, et al., "Waveguide Sub-Wavelength Structures: A Review of Principles and Applications," *Laser & Photonics Reviews* 9 (2015): 25–49, https://doi.org/10.1002/lpor.201400083.

101. X. Zhao, T. Jin, W. Gao, et al., "Embedding $Cs_3Cu_2I_5$ Scintillators Into Anodic Aluminum Oxide Matrix for High-Resolution X-Ray Imaging," *Advanced Optical Materials* 9 (2021): 2101194, https://doi.org/10.1002/adom.202101194.

102. Q. Peng, J. Wei, Z. He, et al., "In Situ Crystallization of $CsPbBr_3$ Nanocrystals Within a Melt-Quenched Glassy Coordination Polymer," *ACS Nano* 19 (2025): 5295–5304, https://doi.org/10.1021/acsnano.4c12049.

103. J. Nie, C. Li, S. Zhou, J. Huang, X. Ouyang, and Q. Xu, "High Photoluminescence Quantum Yield Perovskite/Polymer Nanocomposites for High Contrast X-ray Imaging," *ACS Applied Materials & Interfaces* 13 (2021): 54348–54353, https://doi.org/10.1021/acsami.1c15613.

104. W. Chen, M. Zhou, Y. Liu, et al., “All-Inorganic Perovskite Polymer–Ceramics for Flexible and Refreshable X-Ray Imaging,” *Advanced Functional Materials* 32 (2022): 2107424, https://doi.org/10.1002/adfm.202107424.

105. J. Ghosh, J. O’Neill, M. G. Masteghin, et al., “Surfactant-Dependent Bulk Scale Mechanochemical Synthesis of $CsPbBr_3$ Nanocrystals for Plastic Scintillator-Based X-ray Imaging,” *ACS applied nano materials* 6 (2023): 14980.

106. X. Wu, Z. Guo, S. Zhu, et al., “Ultrathin, Transparent, and High Density Perovskite Scintillator Film for High Resolution X-Ray Microscopic Imaging,” *Advanced Science* 9 (2022): 2200831, https://doi.org/10.1002/advs.202200831.

107. A. Giuri, A. C. Chekkallur, M. Calora, et al., “3D Printed Ultra-Fast Plastic Scintillators Based on Perovskite-Photocurable Polymer Composite,” *Advanced Functional Materials* 35 (2025): 2417653, https://doi.org/10.1002/adfm.202417653.

108. H. Lv, C. Huo, K. Zhang, Q. Hao, and M. Chen, “In-Situ Grown Polymer-Ceramic Scintillator and Applications on X-Ray Multi-Energy Curved Surface Imaging,” *PhotoniX* 6 (2025): 23.

109. X. Hu, P. Yan, P. Ran, et al., “In Situ Fabrication of $Cs_3Cu_2I_5$: Tl Nanocrystal Films for High-Resolution and Ultrastable X-ray Imaging,” *The Journal of Physical Chemistry Letters* 13 (2022): 2862–2870, https://doi.org/10.1021/acs.jpclett.2c00456.

110. K. Xia, P. Ran, W. Wang, et al., “In Situ Preparation of High-Quality Flexible Manganese-Halide Scintillator Films for X-Ray Imaging,” *Advanced Optical Materials* 10 (2022): 2201028, https://doi.org/10.1002/adom.202201028.

111. S. J. Saiji, Y. Tang, S. Wu, L. Stand, Y. Tratsiak, and Y. Dong, “Metal Halide Perovskite Polymer Composites for Indirect X-Ray Detection,” *Nanoscale* 16 (2024): 17654–17682, https://doi.org/10.1039/D4NR02716G.

112. G. Pilania, K. J. McClellan, C. R. Stanek, and B. P. Uberuaga, “Physics-Informed Machine Learning for Inorganic Scintillator Discovery,” *The Journal of Chemical Physics* 148 (2018): 241729, https://doi.org/10.1063/1.5025819.

113. Y. Tuo, Y. Du, C. Chen, et al., “Wearable Radiation Monitoring: Exploration of A_2BX_6 Perovskite Detector Screening Based on Machine Learning and DFT,” *Chemical Engineering Journal* 521 (2025): 166794, https://doi.org/10.1016/j.cej.2025.166794.